NASA TN D-925

TECHNICAL NOTE

D-925

MEASUREMENTS AND CALCULATIONS OF THE EFFECTS OF DISTORTIONS IN THE COLLECTOR SURFACE ON EFFICIENCIES OF UMBRELLA-TYPE SOLAR COLLECTORS

By Victor R. Bond

Langley Research Center
Langley Field, Va.

NATIONAL AERONAUTICS AND SPACE ADMINISTRATION
WASHINGTON

August 1961

A

NATIONAL AERONAUTICS AND SPACE ADMINISTRATION

TECHNICAL NOTE D-925

MEASUREMENTS AND CALCULATIONS OF THE EFFECTS OF DISTORTIONS IN THE COLLECTOR SURFACE ON EFFICIENCIES OF UMBRELLA-TYPE SOLAR COLLECTORS

By Victor R. Bond

SUMMARY

The meridional tensions along the ribs in a Mylar-covered umbrella-type solar collector produce a distortion in the reflecting surface that is detrimental to the image in the focal plane. The investigation reported herein was made to obtain measured and calculated geometric efficiencies of umbrella-type collectors as affected by these surface distortions.

These studies show that if the tension transverse to the ribs is increased relative to the meridional tensions, the distortion is reduced and higher efficiencies can be attained, and if the transverse tension is small, the number of ribs in the collector must be increased for higher efficiencies.

INTRODUCTION

Studies (for example, ref. 1) have shown that umbrella-type structures made up of a number of curved parabolic ribs and covered with a thin material, such as aluminized Mylar, so arranged as to make an approximate paraboloid, would provide mirrors that are capable of collecting solar energy. These umbrella-type structures would be light in weight and easily folded for packaging. The structure would only approximate a perfect paraboloid of revolution, because the surface between any two ribs would be segments of a cylindrical paraboloid. This distortion from the true paraboloidal shape is present regardless of the way in which the material is applied to the ribs. In addition to this distortion, there exists a distortion due to the meridional tensions in the membrane. These tensions are introduced when the material is applied to ribs and serve the purpose of eliminating wrinkles that develop transverse to the ribs. This distortion is toward the axis of symmetry of the approximate paraboloid and causes a

dispersion of the light rays in the theoretical focal plane of the collector. The result is a loss in concentration efficiency.

The effects of the distortion due to the meridional stresses have been studied both experimentally and analytically and the results are presented herein. The effects are studied in the focal plane only, and not with a three-dimensional receiver at the theoretical focal point.

SYMBOLS

a	constant of proportionality, relating shear stress to the coordinate x, lb/cu ft
C	concentration ratio, R^2/r^2
C_1, C_2, C_3	constants of integration
C_S	mean solar constant of radiation, Btu/ft^2-sec
F	a function of x,y,z'
f	theoretical focal length of collector, ft
h	thickness of membrane, mils
K	stress-geometry parameter, af/σ_s,
N	number of ribs in collector
$\dot{Q}$	heat incident in unit time on a unit length along X'-axis, Btu/ft^2-sec
R	radius of collector, ft
r	radius of an aperture in focal plane, ft
S	axis tangent to a meridian, ft
s	arc length along a meridian of paraboloid, ft
s'	arc length along distorted surface, ft
X,Y,Z	coordinate axes of collector, ft
X'	axis in focal plane parallel to X-axis, ft

Y'	axis in focal plane parallel to Y-axis
W	axis normal to the undeformed surface
x,y,z	coordinates along X-, Y-, and Z-axes, respectively, ft
w	coordinate along normal W-axis, ft
x'	coordinate along X'-axis, ft
z'	height of a point on the distorted surface above the XY plane
α	angle between Y-axis and a tangent to the parabola $z = \frac{y^2}{4f}$
ϵ	fraction of initial position by which reflected ray is deviated in the focal plane
η_G	ratio of energy received through an aperture in collector focal plane to total energy that was specularly reflected from collector
θ	rim angle of collector (angle between optic axis and line joining origin of coordinate axes of theoretical focal plane with collector rim)
ϕ	angle between a deviated reflected ray and path of an undeviated ray projected in a horizontal XY plane
ρ	radius of curvature of parabola $z = \frac{y^2}{4f}$, ft
σ_s	tensile stress along a meridian, lb/sq ft
$\sigma_{s,max}$	maximum value of σ_s
$\sigma_{s'}$	tensile stress transverse to ribs, lb/sq ft
τ	shear stress in membrane, lb/sq ft

APPARATUS AND TESTS

The models that were constructed for testing represented one segment of an umbrella-type collector, geometrically similar to that shown in figure 1 and had rigid sides made of 1/4-inch aluminum alloy cut to the desired parabolic shape. The metal sides were attached to a metal base plate to keep the sides from moving with respect to each other. A surface

of Mylar was applied over the area between the two parallel plates as shown in figure 2. The Mylar, being in tension, caused the side plates to deflect in toward each other. This deflection was eliminated by wedging wooden struts between the plates. These struts not only made the sides vertical but also increased the tension transverse to the ribs. Six models were constructed. Three had a rim angle θ of 90° and represented segments from collectors of 30, 60, and 90 ribs, and three had a rim angle θ of 45° and represented segments from collectors of 30, 60, and 90 ribs. All models had a radius R of 36 inches. In building the models, no attempt was made to fix the tensions in the surface at any specific value. The models were constructed so that enough tension parallel to the ribs was present to eliminate surface wrinkles, and enough transverse tension was present to make the surface as flat as possible.

The models were tested on the apparatus shown in figure 3. The test apparatus was a rigid metal stand with three horizontal surfaces supported by six vertical steel rods. The bottom surface was a flat metal plate that served as a support for the models. The top surface was 1/4-inch plate glass and served as a transparent support for the light source. Attached beneath the glass plate was a metal plate in which a grid of 1/8-inch holes had been drilled at 1/2-inch intervals. These holes served as a coordinate system for the narrow-beam light source resting on the glass plate above. The middle surface was another glass plate, the lower surface of which coincided with the intended focal plane of the collector. Glued to the lower surface of this plate was a piece of rectangular coordinate graph paper. The position of the center of an image in the focal plane was read directly from the graph paper and recorded.

The light source was a 25-watt direct-current lamp, the rays of which were collimated with a 13-inch focal-length achromatic lens. A mask blocked off all the light except that through a 1/16-inch hole at the center. The narrow beam of light was made perpendicular to the three horizontal surfaces of the test stand by means of three leveling screws in the base of the lamp and lens housing. The beam of light was thus parallel to the optic axis of the collector.

A schematic diagram of the experimental apparatus is shown in figure 4. The light source was positioned on the glass plate over the desired point on the model surface. The incident light ray was reflected from the model surface onto the grid in the focal plane. The coordinates of the center of the image were read directly from the grid and recorded. The entire surface of the model was surveyed in this manner at regular intervals of area. A plot was made of all the images in the focal plane, and from this plot the experimental geometric efficiency was determined.

RESULTS AND DISCUSSION

The geometric efficiency of a collector η_G, as used in this report, is the ratio of the energy received through an aperture of radius r in the collector focal plane to the total energy that was specularly reflected from the collector. Thus, the geometric efficiency is a measure of the effect of the major surface distortions of the collector at a given concentration ratio. By definition, geometric efficiency does not include losses due to absorptivity of the surface, diffuse reflectivity, minor surface errors, or improper orientation of the collector.

The concentration ratio C is defined as the ratio of the projected collector area πR^2 to the aperture area in the focal plane πr^2. The geometric efficiency is usually presented herein as a function of the concentration ratio.

Parallel light, or a point source at infinity, is used or assumed throughout this investigation. The results are therefore not strictly applicable to the case of a mirror used to concentrate sunlight, since the solar disk subtends an arc of approximately 32 minutes in the vicinity of the earth. Concentration capability in sunlight is consequently always less than in parallel light. However, it can be shown that for a perfect 90-rib umbrella collector, that is, one having no inward curvature of the surface between the ribs, no more than about 3 percent of the reflected sunlight will fall outside of the maximum image diameter formed by parallel light. For less-than-perfect umbrella collectors, and for smaller numbers of ribs, the differences between the results obtained with sunlight and with parallel light will be much less than 3 percent. It is apparent, therefore, that the increased complexity of including the effects of a finite source size is not warranted in an analysis of an umbrella collector. These effects would, of course, have to be included in the analysis of more precise mirrors.

Experimental Calculations

If all image points collected in the focal plane are assumed to represent the same amount of projected collector area, the geometric efficiency may be determined from the data by calculating the ratio of the number of image points in an aperture in the focal plane of radius r to the total number of image points received in the focal plane.

The geometric efficiency η_G was obtained for several aperture radii for each model tested, and the results are presented as a function of concentration ratio in figure 5.

Analytical Results

The complete derivations of the equations used in calculating the theoretical geometric efficiency is given in the appendix. Briefly, the procedure was as follows: The surface equation was derived by considering the tensile forces acting on a small area of the model surface. The surface contour in the XZ plane between two adjacent ribs was found to be parabolic. An example of the surface contour for a 60-rib collector is shown in figure 6. With the surface shape known, the position at which any given light ray falling on the surface would be reflected in the focal plane could be determined and an energy distribution in the focal plane could be obtained. The assumption was made that all the energy from any one segment of the collector would be concentrated along the aperture diameter parallel to the X-axis. This assumption is consistent with the fact that the distortions are so small that essentially only the X projection of the normal to the surface is changed by the distortions. The Y component of the normal changes very little.

An example of the energy distribution for a 60-rib collector over a radius in the focal plane is shown in figure 7. The relations used are given in the appendix. From the energy distribution, the geometric efficiencies were calculated for each radius where it had been determined experimentally. The results are shown in figure 8 compared with the experimental curves. The geometric efficiency is shown plotted against concentration ratio for a particular model and for a range of the stress-geometry parameter K of 0, 2, and 4.

The stress-geometry parameter K is shown in the appendix to be a function of the maximum stress ratio $\frac{\sigma_{s,max}}{\sigma_{s'}}$, which occurs at the vertex of the umbrella segment, and of the geometry. It is shown that the parameter K is $0.556\frac{\sigma_{s,max}}{\sigma_{s'}}$ for a collector with a 90° rim angle $\left(\frac{R}{f} = 2\right)$ and is $1.216\frac{\sigma_{s,max}}{\sigma_{s'}}$ for a collector with a 45° rim angle $\left(\frac{R}{f} = 0.829\right)$.

Comparison of Experimental and Analytical Results

No attempt was made to measure the stresses in any of the collector models. The transverse tension was increased by addition of struts between the sides of the model until very little curvature could be detected visually. From figure 8 it is apparent that the

90°-rim-angle models had smaller stress-geometry parameters than did the 45°-rim-angle models. This result is consistent with the result shown in the appendix; namely, that K should be smaller for the model with a 90°-rim angle than with a 45° rim angle, if the maximum tension ratio is assumed to be the same in both models.

For the models with rim angles of 90°, the experimental curves lie, in general, between the calculated curves with stress parameters K of 2 and 4 for the models of segments from 60- and 90-rib collectors, and between the calculated curves with stress parameters K of 0 and 2 for the segments from a 30-rib collector.

For the models with rim angles of 45°, the experimental curves lie in the region to the left of the calculated curves with stress parameter K of 4 for the models of segments from 60- and 90-rib collector, and between the calculated curves with stress parameters K of 2 and 4 for the segment from the 30-rib collector.

The experimental curves are seen to be at least 20 percent less than the maximum calculated geometric efficiencies, where the stress-geometry parameter is zero, in spite of the care to flatten the surface contours of the model. The experimental curves are lower primarily because of the nature of the surface curvature. A secondary effect is reduction of efficiency caused by dispersion of a few points which fell on local irregularities of the membrane.

For a given concentration ratio and configuration, the efficiency decreases with increasing stress parameter, as shown in figure 8. For example, with a 60-rib 45°-rim-angle collector at a concentration ratio C of 1,000, the geometric efficiency is 0.83, 0.66, and 0.53 for stress parameters of 0, 2, and 4, respectively.

Figure 9 presents cross plots of the data from figure 8 at a concentration ratio of 1,000. The geometric efficiency is presented as a function of the number of ribs N. It is seen that the 45°-rim-angle models have higher theoretical efficiencies than the 90°-rim-angle models for the same stress-geometry parameter. However, the experimental geometric efficiencies are about the same at a concentration ratio of 1,000. Experimentally, the geometric efficiency increases linearly over the range of ribs from 30 to 90. A slight linear extrapolation of the experimental curves shows that in order to provide an efficiency of 0.80 at a concentration ratio of 1,000, a collector would require about 106 ribs for a 45° rim angle and about 110 ribs for a 90° rim angle.

Also, from figure 9, it is seen that a lower limit to the number of ribs necessary for a usable calculated efficiency of 0.90 at a

concentration of 1,000 exists. For example, in the case of 45°-rim-angle collectors (fig. 9(a)), a collector with a stress parameter K of 2 must have 88 ribs and a collector with a stress-geometry parameter K of 4 must have 106 ribs. In order to attain high geometric efficiency, collectors must be constructed with small stress-geometry parameters, or with a large number of ribs.

CONCLUSIONS

The effects of distortions in the collector surface on the efficiencies of umbrella-type solar collectors have been investigated experimentally and theoretically, and the following conclusions are indicated:

1. For a given model and concentration ratio, the theoretical geometric efficiency decreases as the stress-geometry parameter K increases. For example, the maximum theoretical geometric efficiency attainable for stress-geometry parameter zero at a concentration of 1,000 is 0.83 for a 60-rib collector with 45° rim angle. When the stress-geometry parameter has values of 2 and 4, the efficiencies attainable are reduced to 0.66 and 0.53, respectively.

2. For an umbrella-type solar collector to have high efficiency, it must be constructed so that either the stress-geometry parameter is small (that is, the transverse tension is large) or the number of ribs is large. For a collector with a rim angle of 45°, an efficiency of 0.90 at a concentration of 1,000 may be obtained with 88 ribs and a stress-geometry parameter of 2, or with 106 ribs and a stress-geometry parameter of 4.

3. Calculations show that collectors with 45° rim angles give higher geometric efficiencies than the collectors with 90° rim angles for the same concentration and stress-geometry parameter. Experimentally, there was little difference in the geometric efficiencies at a concentration ratio of 1,000 in the range between 30 to 90 ribs. The 90°-rim-angle models had smaller stress-geometry parameters than did the 45°-rim-angle models. It was also shown by calculation that the 90°-rim-angle collectors should have smaller stress-geometry parameters than the 45°-rim-angle collectors.

The experimental geometric efficiencies were in all cases about 20 percent below the maximum calculated efficiencies, which were for collectors with stress-geometry parameter of zero.

Langley Research Center,
National Aeronautics and Space Administration,
Langley Field, Va., May 22, 1961.

APPENDIX

ANALYTICAL DERIVATIONS

Derivation of Surface Equation

The equation of the surface between the two parabolic ribs of an umbrella-type collector is found by considering the forces that act upon a small element of the surface ds ds'. (See sketches 1 and 2.)

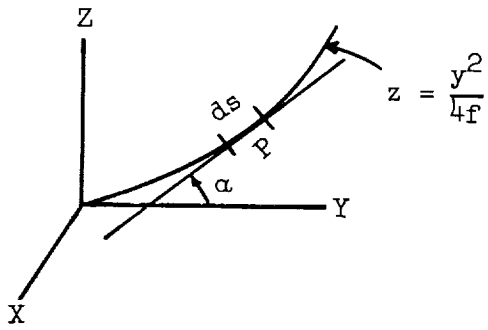

Sketch 1

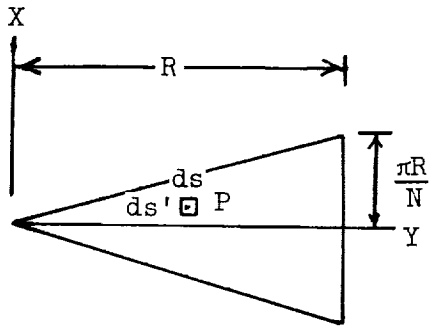

Sketch 2

If the number of ribs is large, 30 or greater, then the projection of the segment in the XY plane is a good approximation to a triangle of height R and base $2\pi R/N$.

The forces on the element are resolved (as shown in sketch 3) along the orthogonal axes, W, S, and X which have their origin at the center of the initial position of the element.

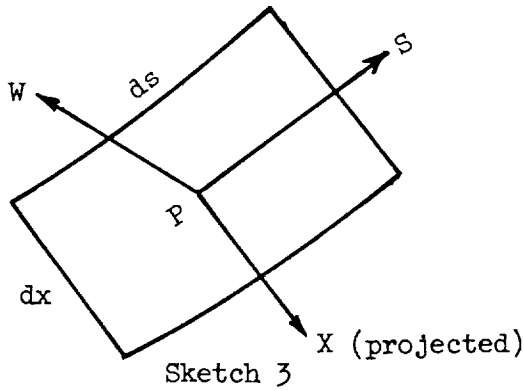

Sketch 3

The axis W is normal to the undeformed surface at the point P; S is tangent to the surface at P and lies in a plane parallel to the YZ plane.

Consider the stresses acting on the surface element as shown in sketch 4. Assume that the angles made by the stresses with the axes S and X are small.

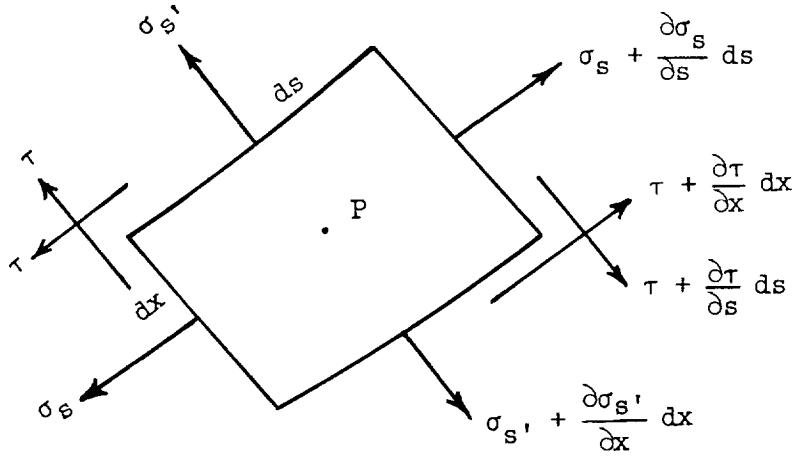

Sketch 4

For equilibrium in the X-direction,

$$\left[\sigma_{s'} + \frac{\partial \sigma_{s'}}{\partial x} dx - \sigma_{s'}\right] h\, ds + \left[\tau + \frac{\partial \tau}{\partial s} ds - \tau\right] h\, dx = 0$$

or

$$\frac{\partial \sigma_{s'}}{\partial x} + \frac{\partial \tau}{\partial s} = 0 \qquad (1)$$

For equilibrium in the S-direction,

$$\left[\sigma_s + \frac{\partial \sigma_s}{\partial s} ds - \sigma_s\right] h\, dx + \left[\tau + \frac{\partial \tau}{\partial x} dx - \tau\right] h\, ds = 0$$

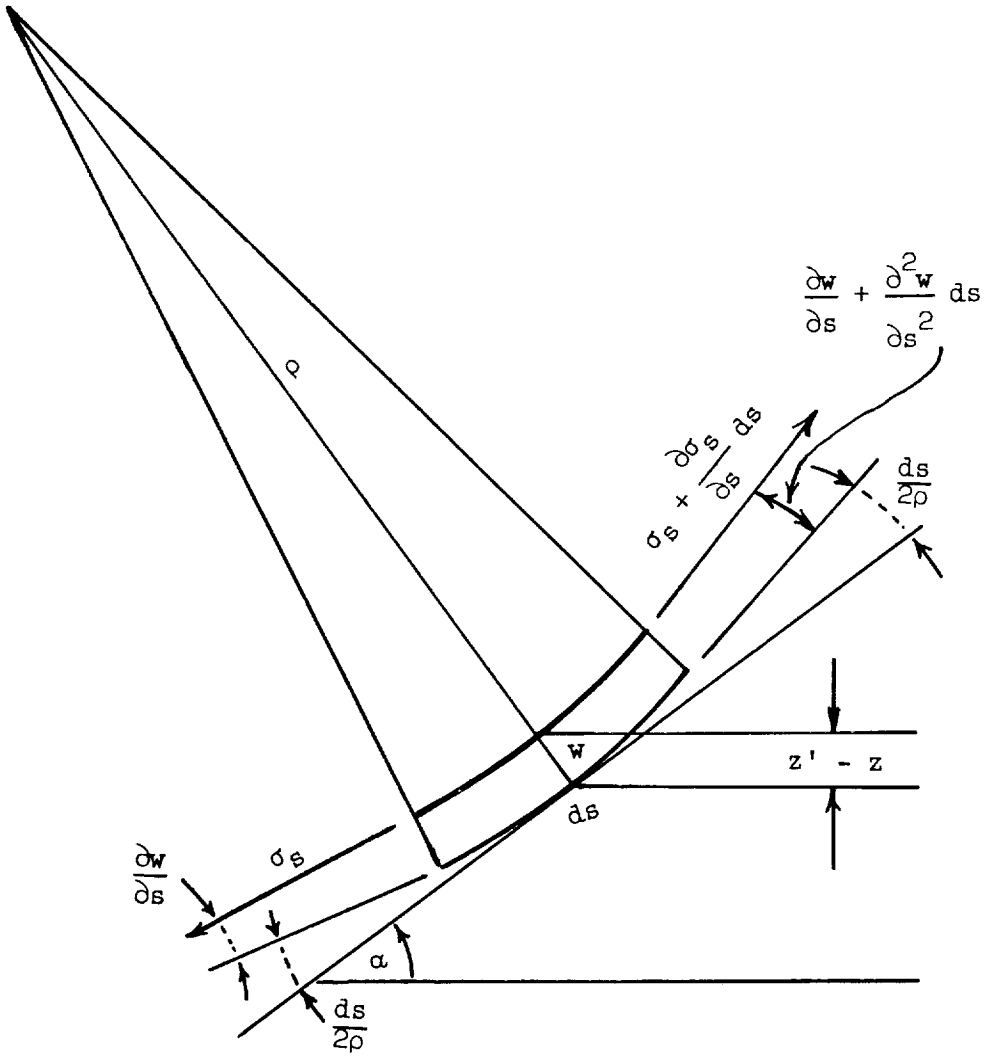

Sketch 5

if two small terms due to the curvature of the ribs are neglected. This equation simplifies to

$$\frac{\partial \sigma_s}{\partial s} + \frac{\partial \tau}{\partial x} = 0 \qquad (2)$$

For equilibrium along the normal, or W, direction, several force components are to be taken into account. The normal components due to stresses σ_s, $\sigma_{s'}$, and τ are as follows:

(a) The principal part of the normal component is due to the curvature of ribs. (See sketch 5.) This component becomes, for rib radius of curvature ρ,

$$\left[\left(\sigma_s + \frac{\partial \sigma_s}{\partial s}\, ds\right)\sin\left(\frac{ds}{2\rho}\right) + \sigma_s \sin\left(\frac{ds}{2\rho}\right)\right] h\, dx = \sigma_s h \frac{ds\, dx}{\rho}$$

since $ds/2\rho$ is a small angle and terms in $(ds)^2$ are neglected.

(b) The normal component due to the stress σ_s acts in the deformed surface. This component, as seen from sketch 5, is

$$\left(\sigma_s + \frac{\partial \sigma_s}{\partial s}\, ds\right)\left(\frac{\partial w}{\partial s} + \frac{\partial^2 w}{\partial s^2}\, ds\right) h\, dx - \sigma_s \frac{\partial w}{\partial s}\, h\, dx = h\left[\frac{\partial}{\partial s}\left(\sigma_s \frac{\partial w}{\partial s}\right)\right] dx\, ds$$

if terms in $(ds)^2$ are neglected.

(c) Also present is a normal component due to $\sigma_{s'}$. This component is found in a manner analogous with that due to σ_s as $h\, ds\, dx\left[\frac{\partial}{\partial x}\left(\sigma_{s'} \frac{\partial w}{\partial x}\right)\right]$.

(d) A normal component due to the shear stress τ acting in the membrane is illustrated in sketch 6.

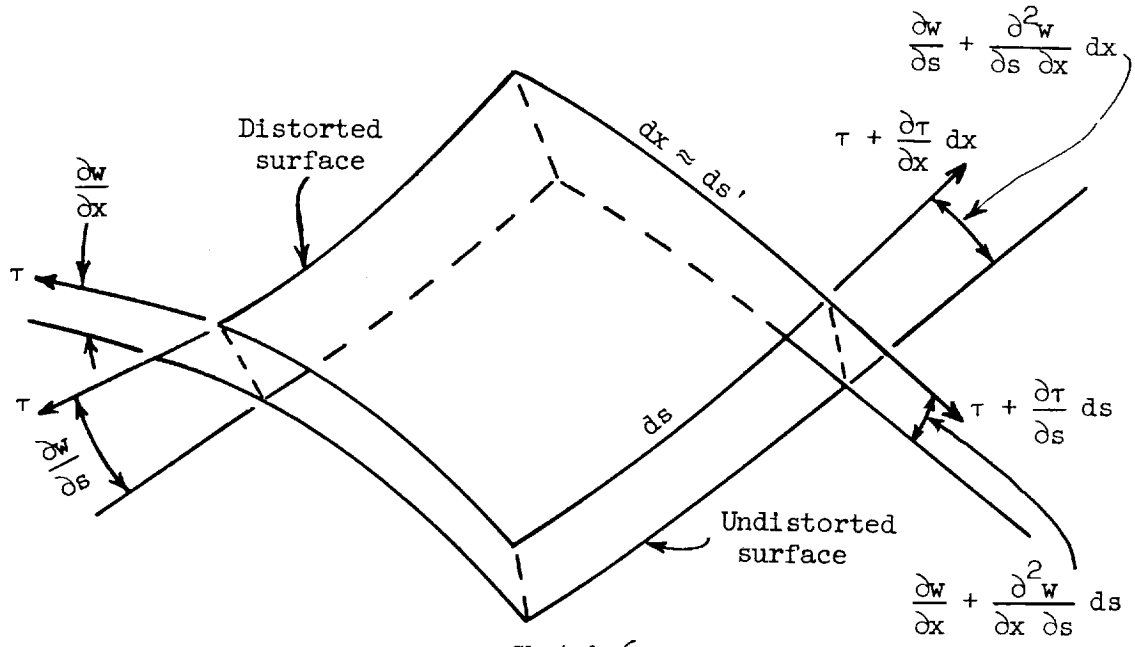

Sketch 6

This component becomes,

$$\left[\left(\tau + \frac{\partial \tau}{\partial x}\,dx\right)\left(\frac{\partial w}{\partial s} + \frac{\partial^2 w}{\partial s\,\partial x}\,dx\right) - \tau\,\frac{\partial w}{\partial s}\right]h\,ds$$

$$+\left[\left(\tau + \frac{\partial \tau}{\partial s}\,ds\right)\left(\frac{\partial w}{\partial x} + \frac{\partial^2 w}{\partial x\,\partial s}\,ds\right) - \tau\,\frac{\partial w}{\partial x}\right]h\,dx = \left[\frac{\partial}{\partial x}\left(\tau\,\frac{\partial w}{\partial s}\right) + \frac{\partial}{\partial s}\left(\tau\,\frac{\partial w}{\partial x}\right)\right]h\,ds\,dx$$

where terms in $(ds)^2$ and $(dx)^2$ are neglected.

Collecting all normal components found in the preceding paragraphs (a), (b), (c), and (d) for equilibrium in the normal direction gives

$$h\,dx\,ds\left[\frac{\partial}{\partial s}\left(\sigma_s\,\frac{\partial w}{\partial s}\right)+\frac{\partial}{\partial x}\left(\sigma_{s'}\,\frac{\partial w}{\partial x}\right)\right]$$

$$+\,h\,dx\,ds\left[\frac{\partial}{\partial x}\left(\tau\,\frac{\partial w}{\partial s}\right)+\frac{\partial}{\partial s}\left(\tau\,\frac{\partial w}{\partial x}\right)\right]+\frac{\sigma_s}{\rho}\,h\,dx\,ds=0$$

Rearranging and dividing this equation by $h\,dx\,ds$ yields

L
1
3
0
9

$$\frac{\partial}{\partial s}\left[\sigma_s\,\frac{\partial w}{\partial s}+\tau\,\frac{\partial w}{\partial x}\right]+\frac{\partial}{\partial x}\left[\sigma_{s'}\,\frac{\partial w}{\partial x}+\tau\,\frac{\partial w}{\partial s}\right]+\frac{\sigma_s}{\rho}=0 \tag{3}$$

Inasmuch as the deflections are small, it is assumed that $\frac{\partial w}{\partial s}\approx 0$. The normal force in equation (3) then becomes

$$\frac{\partial}{\partial s}\left(\tau\,\frac{\partial w}{\partial x}\right)+\frac{\partial}{\partial x}\left(\sigma_{s'}\,\frac{\partial w}{\partial x}\right)+\frac{\sigma_s}{\rho}=0$$

It is also assumed that the stress $\sigma_{s'}$ does not vary with x; that is, $\frac{\partial \sigma_{s'}}{\partial x}\approx 0$. This assumption signifies that the tensile stress across the rib in the x direction at any point remains constant when the surface is deformed; therefore, for equilibrium in the normal direction,

$$\sigma_{s'}\,\frac{\partial^2 w}{\partial x^2}+\frac{\partial}{\partial s}\left(\tau\,\frac{\partial w}{\partial x}\right)+\frac{\sigma_s}{\rho}=0 \tag{4}$$

Equations (1), (2), and (4) are the equilibrium equations for the membrane.

With the assumption that $\frac{\partial \sigma_{s'}}{\partial x}\approx 0$, equation (1) becomes $\frac{\partial \tau}{\partial s}=0$. This means that τ cannot be a function of s or of y since s depends on y. Therefore, $\tau=\tau(x)$.

Assume now that $\tau = ax$. This condition allows the shear stress to vanish at the center of the surface and to be a maximum at the boundary. If $\tau = ax$, then from equation (2),

$$\frac{\partial \sigma_s}{\partial s} = - \frac{\partial \tau}{\partial x} = -a \tag{5}$$

Thus, σ_s depends upon s and y. Equation (4) may be written

$$\sigma_{s'} \frac{\partial^2 w}{\partial x^2} + \tau \frac{\partial}{\partial s}\left(\frac{\partial w}{\partial x}\right) + \frac{\sigma_s}{\rho} = 0 \tag{6}$$

Since

$$\frac{\partial^2 w}{\partial x^2} = \frac{\partial}{\partial x}\left(\frac{\partial w}{\partial x}\right) \gg \frac{\partial}{\partial s}\left(\frac{\partial w}{\partial x}\right)$$

and since from equation (2), it is seen that σ_s and τ are of the same order of magnitude, the second term of equation (6) may be neglected compared with the first. Equation (4) then becomes

$$\sigma_{s'} \frac{\partial^2 w}{\partial x^2} + \frac{\sigma_s}{\rho} = 0 \tag{7}$$

Because $\sigma_{s'}$ does not depend on x, and because σ_s and ρ are functions of y, equation (7) may be integrated to give

$$\sigma_{s'} \frac{\partial w}{\partial x} = - \frac{\sigma_s}{\rho} x + C_1 \tag{8}$$

Since w is symmetrical with respect to x, $\left(\frac{dw}{dx}\right)_{x=0} = 0$, so that $C_1 = 0$. Integration of equation (8) gives

$$w = - \frac{1}{2} \frac{\sigma_s}{\sigma_{s'}\rho} x^2 + C_2 \tag{9}$$

At the boundary, where $x = \frac{\pi}{N} y$, $w = 0$, and therefore

$$C_2 = \frac{1}{2} \frac{\sigma_s}{\sigma_{s'}\rho} \frac{\pi^2}{N^2} y^2 \tag{10}$$

Therefore, the normal deflections (eq. (9)) are given by

$$w = \frac{1}{2} \frac{\sigma_s}{\sigma_{s'}, \rho} \left(\frac{\pi^2}{N^2} y^2 - x^2 \right) \tag{11}$$

The vertical deflections are seen from sketch 5 to be,

$$z' - z = w \cos \alpha \tag{12}$$

where

$$\cos \alpha = \frac{dy}{ds} = \frac{1}{\left[1 + \left(\frac{dz}{dy} \right)^2 \right]^{1/2}} \tag{13}$$

Since $z = \frac{y^2}{4f}$

$$\frac{dz}{dy} = \frac{y}{2f}$$

and, therefore, equation (13) becomes

$$\cos \alpha = \left(\frac{1}{1 + \frac{y^2}{4f^2}} \right)^{1/2}$$

The radius of curvature ρ is defined by

$$\rho = \frac{\left[1 + \left(\frac{dz}{dy} \right)^2 \right]^{3/2}}{\frac{d^2 z}{dy^2}}$$

$$= 2f \left(1 + \frac{y^2}{4f^2} \right)^{3/2}$$

With these substitutions for $\cos \alpha$ and ρ in equation (12), the vertical deflections $z' - z$ become

$$z' - \frac{y^2}{4f} = \frac{1}{4f}\frac{\sigma_s}{\sigma_{s'}}\frac{\left(\frac{\pi^2}{N^2}y^2 - x^2\right)}{\left(1 + \frac{y^2}{4f^2}\right)^2} \tag{14}$$

Evaluation of Stress σ_s and Stress-Geometry Parameter K

From the assumption that $\tau = ax$ and equation (2), the stress σ_s may be found. Since equation (5) shows that $\frac{\partial \sigma_s}{\partial s} = -a$,

$$\sigma_s = -a \int ds$$

$$= -a \int \left(1 + \frac{y^2}{4f^2}\right)^{1/2} dy \tag{15}$$

When this equation is integrated,

$$\sigma_s = -af\left\{\frac{y}{2f}\left(1 + \frac{y^2}{4f^2}\right)^{1/2} + \log_e\left[\frac{y}{2f} + \left(1 + \frac{y^2}{4f^2}\right)^{1/2}\right]\right\} + afC_3 \tag{16}$$

When $y = R$, $\sigma_s = 0$, and the constant C_3 becomes

$$C_3 = \frac{R}{2f}\left(1 + \frac{R^2}{4f^2}\right)^{1/2} + \log_e\left[\frac{R}{2f} + \left(1 + \frac{R^2}{4f^2}\right)^{1/2}\right] \tag{17}$$

The stress σ_s (eq. (16)) is therefore

$$\sigma_s = af\left\{\frac{R}{2f}\left(1 + \frac{R^2}{4f^2}\right)^{1/2} - \frac{y}{2f}\left(1 + \frac{y^2}{4f^2}\right)^{1/2} + \log_e\left[\frac{\frac{R}{2f} + \left(1 + \frac{R^2}{4f^2}\right)^{1/2}}{\frac{y}{2f} + \left(1 + \frac{y^2}{4f^2}\right)^{1/2}}\right]\right\} \tag{18}$$

A convenient constant for making calculations may be found from equation (18). At the origin ($x = y = z' = 0$), the stress σ_s takes on its maximum value

$$\sigma_{s,max} = af \left\{ \frac{R}{2f}\left(1 + \frac{R^2}{4f^2}\right)^{1/2} + \log_e\left[\frac{R}{2f} + \left(1 + \frac{R^2}{4f^2}\right)^{1/2}\right] \right\}$$

Dividing this equation by $\sigma_{s'}$ and solving for $af/\sigma_{s'}$, which is defined as K, gives

$$K = \frac{af}{\sigma_{s'}} = \frac{\sigma_{s,max}/\sigma_{s'}}{\frac{R}{2f}\left(1 + \frac{R^2}{4f^2}\right)^{1/2} + \log_e\left[\frac{R}{2f} + \left(1 + \frac{R^2}{4f^2}\right)^{1/2}\right]} \qquad (19)$$

The parameter K thus depends upon the maximum stress ratio $\sigma_{s,max}/\sigma_{s'}$ and the geometry of the umbrella segment R/f.

For the two values of R/f investigated herein, K is obtained as:

For $\theta = 45^\circ$ or $\frac{R}{f} = 0.829$,

$$K = 1.216 \frac{\sigma_{s,max}}{\sigma_{s'}}$$

For $\theta = 90^\circ$ or $\frac{R}{f} = 2.000$,

$$K = 0.556 \frac{\sigma_{s,max}}{\sigma_{s'}}$$

Determination of the Deviation of a Point Image in Focal Plane

A ray of light incident upon the deformed surface is reflected to a point in the focal plane, as shown in sketch 7.

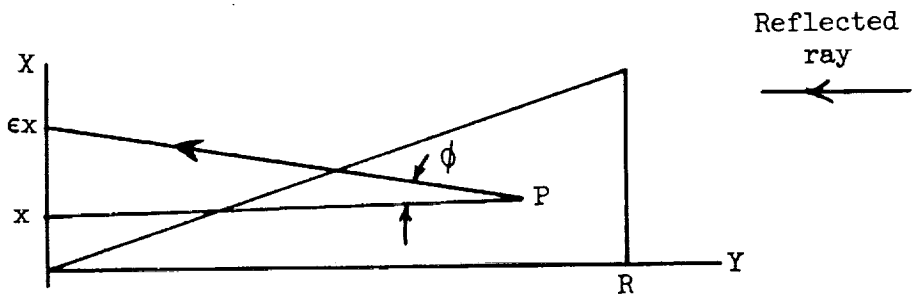

Sketch 7

The reflected ray lies in the plane containing the normal to the surface and the incident ray.

The projections in the XY plane of the normal to the deformed surface are proportional to the directional derivatives, $\partial F/\partial x$ and $\partial F/\partial y$, of the normal. The projections of the reflected ray in the XY plane coincide with the projections of the normal and are thus also proportional to $\partial F/\partial x$ and $\partial F/\partial y$.

The function F is merely equation (14) rewritten as

$$F(x,y,z') = z' - \frac{y^2}{4f} - \frac{1}{4f}\frac{\sigma_s}{\sigma_{s'}}\frac{\left(\frac{\pi^2}{N^2}y^2 - x^2\right)}{\left(1 + \frac{y^2}{4f^2}\right)^2}$$

The directional derivatives $\partial F/\partial x$ and $\partial F/\partial z'$ are found immediately to be

$$\frac{\partial F}{\partial x} = \frac{\frac{\sigma_s}{\sigma_{s'}}x}{2f\left(1 + \frac{y^2}{4f^2}\right)^2}$$

and

$$\frac{\partial F}{\partial z'} = 1$$

The directional derivative $\partial F/\partial y$ is found from the relation,

$$\frac{\partial F/\partial y}{\partial F/\partial z'} = -\frac{\partial z'}{\partial y} = \frac{\partial F}{\partial y}$$

since $\frac{\partial F}{\partial z'} = 1$. Inasmuch as the deflections $z' - z$ are small, the slope $\partial z/\partial y$ of the parabola $z = \frac{y^2}{4f}$ is nearly the same as $\partial z'/\partial y$. That is, since

$$z' - z = z' - \frac{y^2}{4f} \approx 0$$

$$\frac{\partial z}{\partial y} = \frac{\partial z'}{\partial y} = \frac{y}{2f}$$

Consequently, the directional derivative $\partial F/\partial y$ becomes

$$\frac{\partial F}{\partial y} = -\frac{y}{2f}$$

From sketch 7, the angle ϕ that the deviated reflected ray makes with the undeviated ray in the XY plane is

$$\tan \phi = -\frac{\partial F/\partial x}{\partial F/\partial y} \approx \phi$$

since ϕ is a small angle. So the angle ϕ becomes

$$\phi = \frac{\frac{\sigma_s}{\sigma_{s'}} x}{y\left(1 + \frac{y^2}{4f^2}\right)^2}$$

The deviation along the X'-axis in the focal plane is

$$\epsilon x = y\phi$$

Therefore,

$$\epsilon x = \frac{\frac{\sigma_s}{\sigma_{s'}} x}{\left(1 + \frac{y^2}{4f^2}\right)^2}$$

The coordinate x' of the deviated ray in the focal plane is

$$x' = x + \epsilon x$$

or

$$x' = x\left[1 + \frac{\sigma_s/\sigma_{s'}}{\left(1 + \frac{y^2}{4f^2}\right)^2}\right] \qquad (20)$$

An investigation as to the deviations of the reflected ray along the Y- and Z-axis near the focal plane may be made by comparing the directional derivatives of the normal to an undistorted surface with those just calculated for the normal to the distorted surface. For an undistorted surface,

$$z' = z = \frac{y^2}{4f}$$

and

$$F(x,y,z') = z' - \frac{y^2}{4f} = 0$$

The directional derivatives of the normal to this surface are:

$$\frac{\partial F}{\partial x} = 0$$

$$\frac{\partial F}{\partial y} = - \frac{y}{2f}$$

and

$$\frac{\partial F}{\partial z'} = 1$$

For the distorted surface it has been shown that

$$\frac{\partial F}{\partial x} = \frac{\frac{\sigma_s}{\sigma_{s'}} x}{2f \left(1 + \frac{y^2}{4f^2}\right)^2}$$

$$\frac{\partial F}{\partial y} \approx - \frac{y}{2f}$$

and

$$\frac{\partial F}{\partial z'} = 1$$

It is seen, then, that the normal projections do not change at all along Z and are very nearly the same along Y. The only significant change in the normal is along the X-axis. It is assumed throughout this report, then, that all of the reflected rays will fall on the X-axis.

Calculation of Flux Distribution over a Diameter in the Focal Plane

On the surface between the two ribs, there is some locus of points, beginning at $y = R$ and terminating on a rib at $y = y_0$, which will always reflect a ray of light to the same point on the X'-axis in the focal plane. (See sketch 8.)

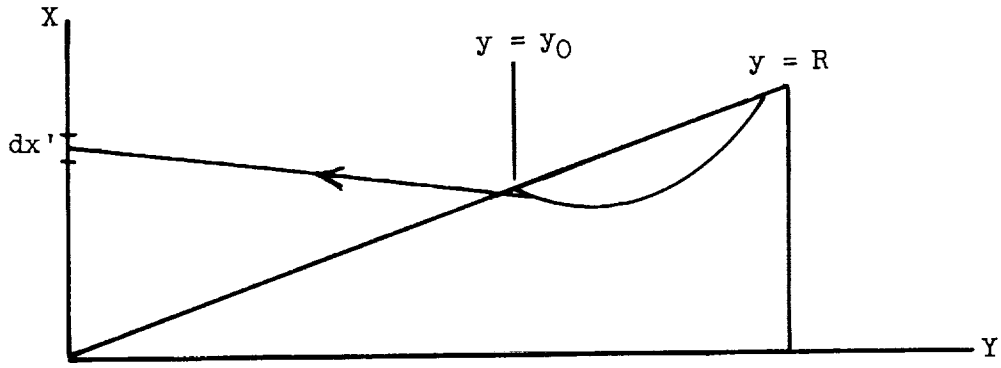

Sketch 8

From the law of conservation of energy

$$C_S \, dx \, dy = d\dot{Q} \, dx'$$

or

$$\frac{d\dot{Q}}{C_S} = \frac{dx}{dx'} \, dy$$

From equation (20)

$$\frac{dx'}{dx} = 1 + \epsilon$$

where

$$\epsilon = \frac{\sigma_s/\sigma_{s'}}{\left(1 + \frac{y^2}{4f^2}\right)^2}$$

Then,

$$\frac{\dot{Q}}{C_S} = \int_{y_0}^{R} \frac{dy}{1 + \epsilon}$$

$$= \int_{y_0}^{R} \frac{dy}{1 + \dfrac{\sigma_s/\sigma_{s'}}{\left(1 + \dfrac{y^2}{4f^2}\right)^2}}$$

Or, in nondimensional form,

$$\frac{\dot{Q}}{C_S f} = 2 \int_{y_0/2f}^{R/2f} \frac{d(y/2f)}{1 + \dfrac{\sigma_s/\sigma_{s'}}{\left(1 + \dfrac{y^2}{4f^2}\right)^2}} \tag{21}$$

This equation (eq. (21)) has been evaluated by graphical integration. The values of $\dot{Q}/C_S f$ obtained are plotted as functions of x'/f in figure 7. The quantity x'/f is obtained from equation (20), which has been nondimensionalized to give

$$\frac{x'}{f} = \frac{\pi}{N} \frac{y_0}{f} \left[1 + \frac{\sigma_s/\sigma_{s'}}{\left(1 + \dfrac{y^2}{4f^2}\right)^2} \right] \tag{22}$$

Calculation of Geometric Efficiency and Concentration Ratio

The geometric efficiency as a function of concentration ratio is obtainable from relations shown in equations (21) and (22) as described in the following paragraphs.

First, plot of $\dot{Q}/C_S f$ against x'/f as shown in sketch 9.

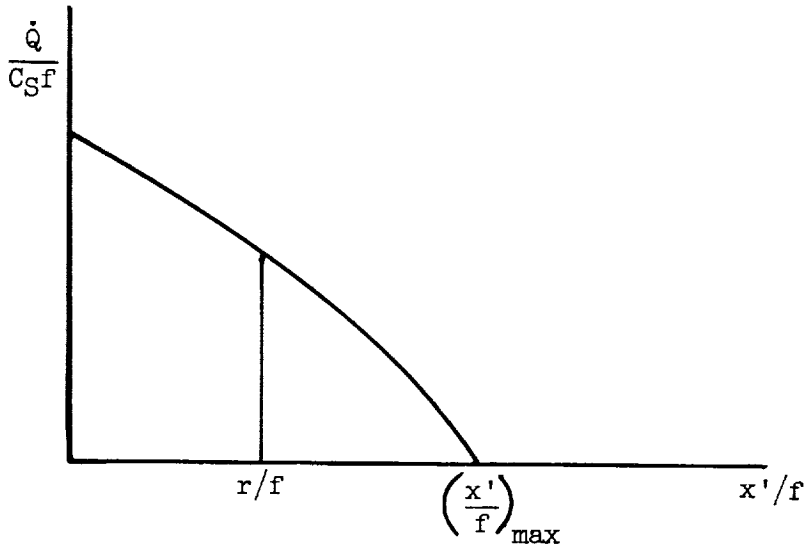

Sketch 9

The total nondimensional energy absorbed by the radius in the focal plane is

$$\int_0^{(x'/f)_{max}} \left(\frac{\dot{Q}}{C_S f}\right) d\frac{x'}{f}$$

The energy received by the radius, when only a portion of the radius out to $\frac{x'}{f} = \frac{r}{f}$ is exposed is

$$\int_0^{r/f} \left(\frac{\dot{Q}}{C_S f}\right) d\frac{x'}{f}$$

The geometric efficiency is then given by

$$\eta_G = \frac{\int_0^{r/f} \left(\frac{\dot{Q}}{C_S f}\right) d\,\frac{x'}{f}}{\int_0^{(x'/f)_{max}} \left(\frac{\dot{Q}}{C_S f}\right) d\frac{x'}{f}}$$

This relation was solved by graphical methods for a particular segment with a given stress-geometry parameter K. The geometric efficiency was plotted as a function of the concentration ratio C where,

$$C = \frac{(R/f)^2}{(r/f)^2}$$

Since the same integration could be obtained for the total number N of the collector segments, the total geometric efficiency is the same as that for one segment.

REFERENCE

1. Von Doenhoff, Albert E., and Hallissy, Joseph M., Jr.: Systems Using Solar Energy For Auxiliary Space Vehicle Power. Rep. No. 59-40, Inst. Aero. Sci., Jan. 1959.

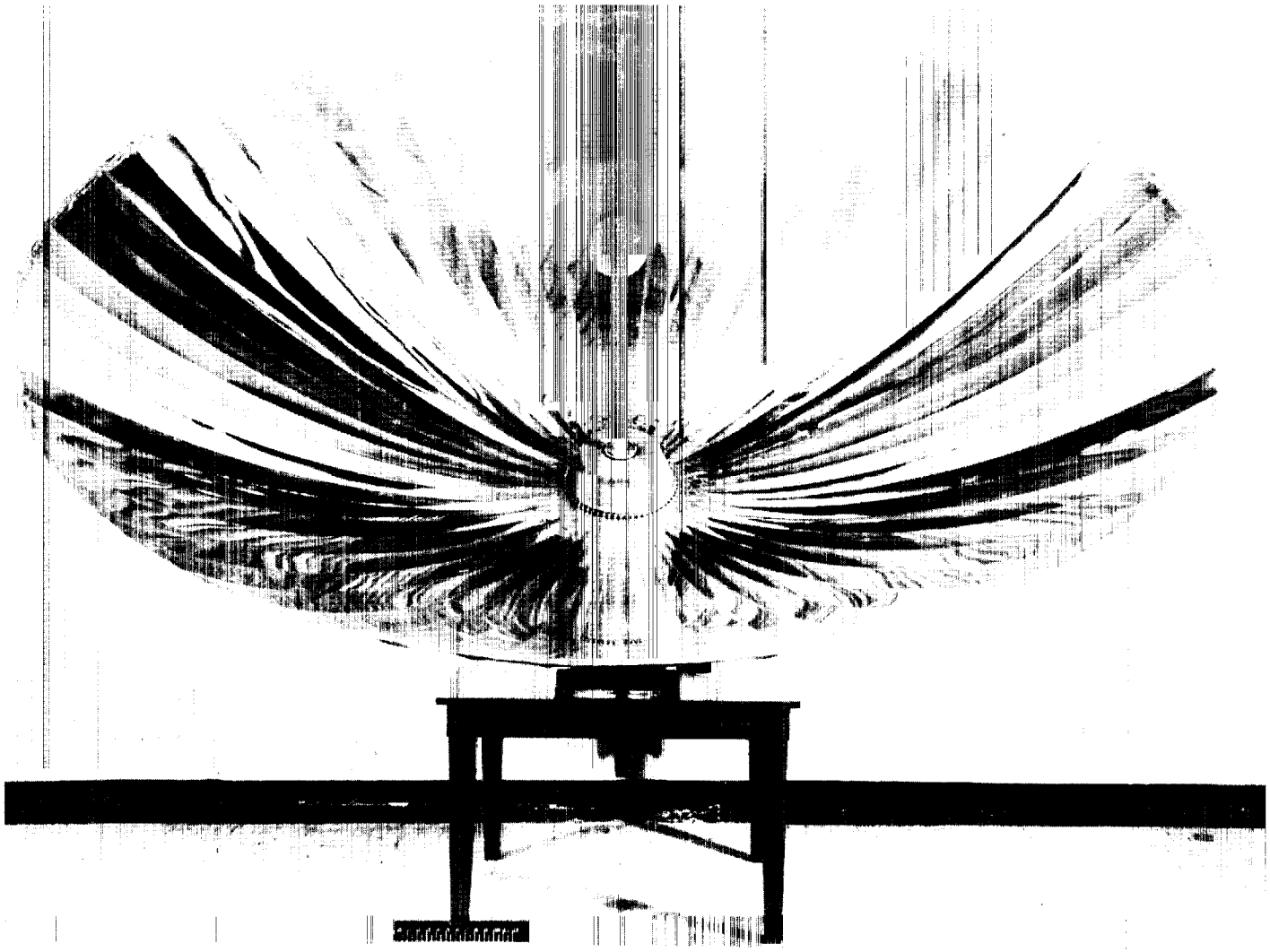

L-60-1409

Figure 1.- Umbrella-type collector. 10-foot diameter; 60 ribs; rim angle, 90°.

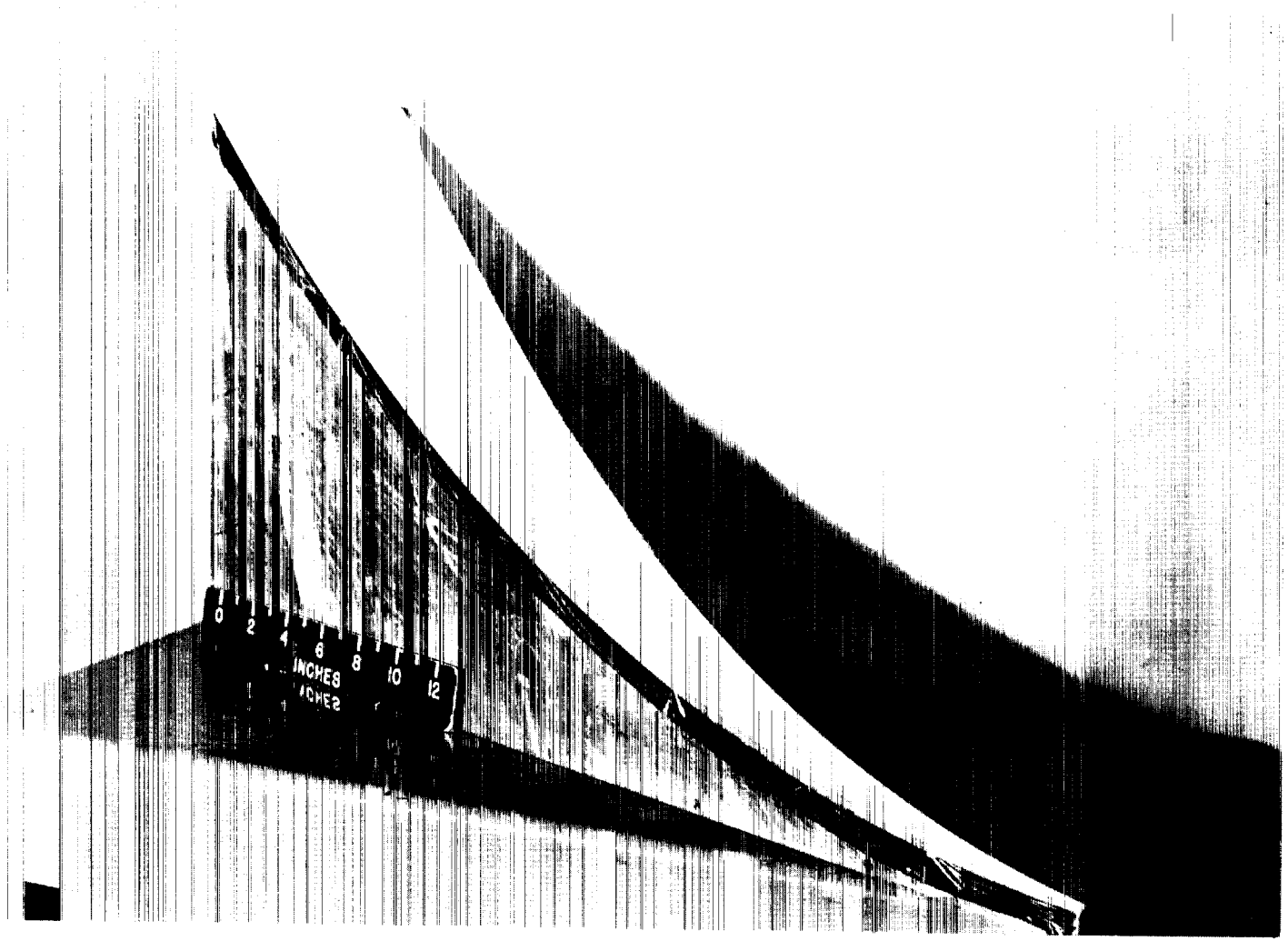

L-59-8514

Figure 2.- Experimental collector-model segment. 30-rib segment; rim angle, 90°.

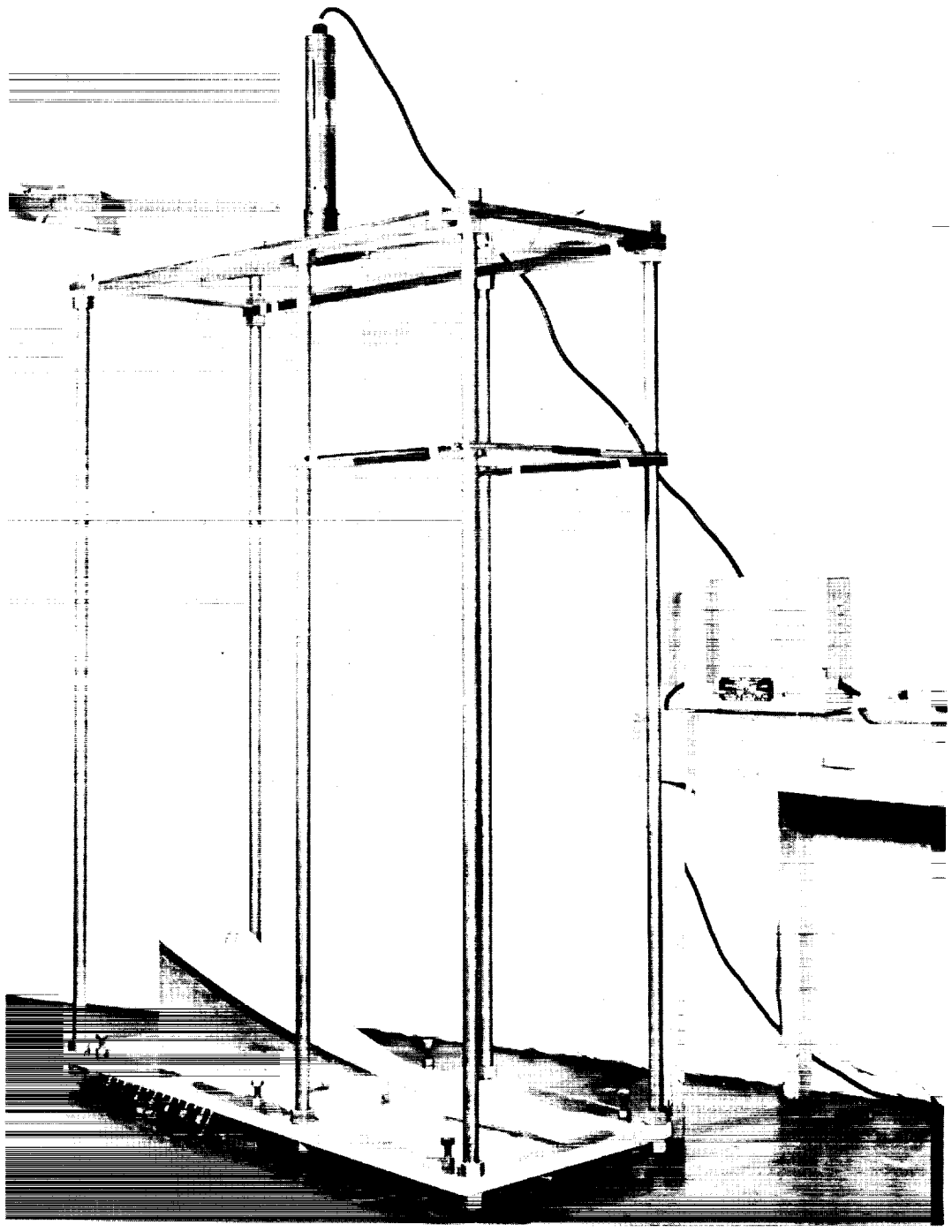

Figure 3.- Experimental test setup. L-59-8509

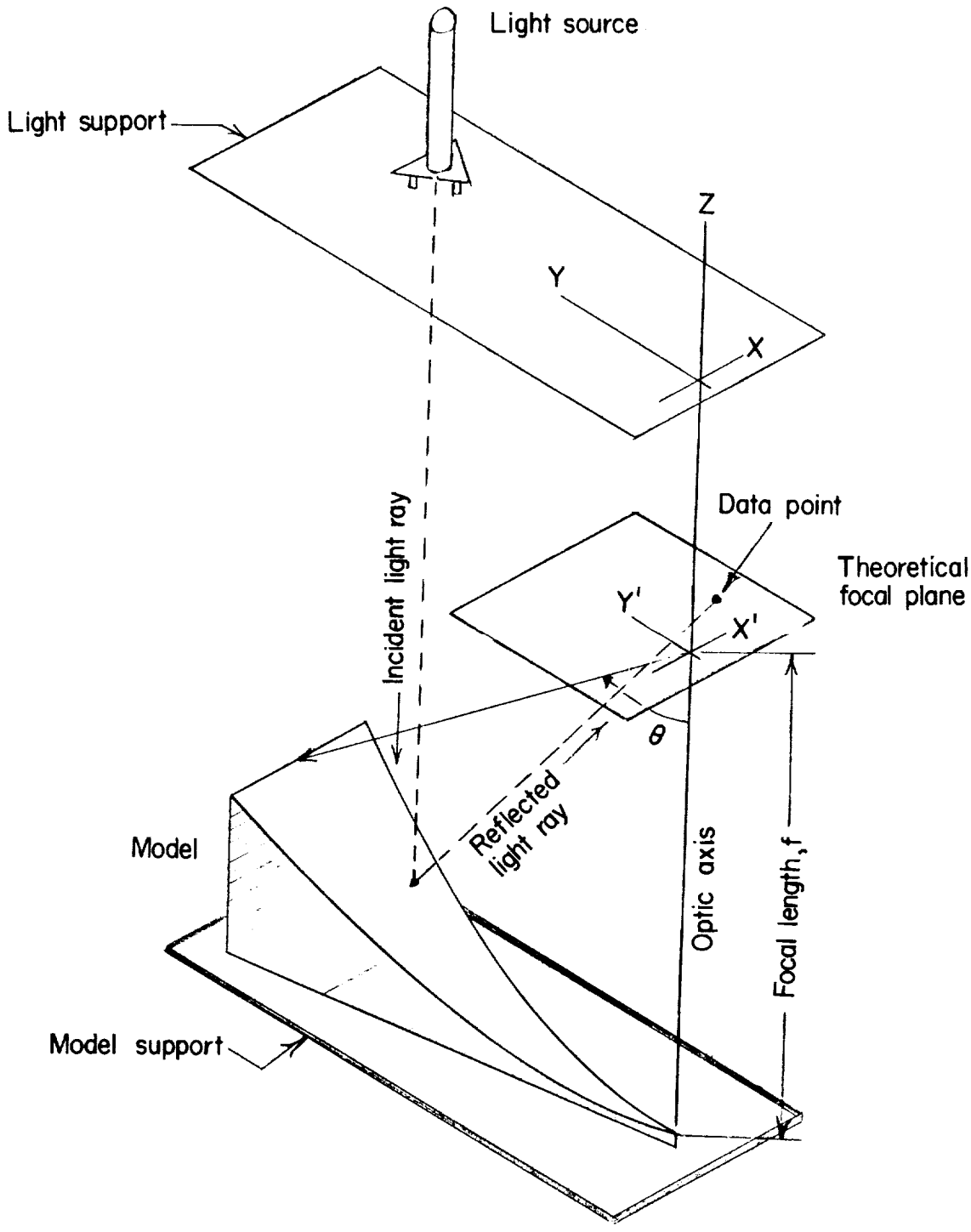

Figure 4.- Schematic diagram of experimental apparatus.

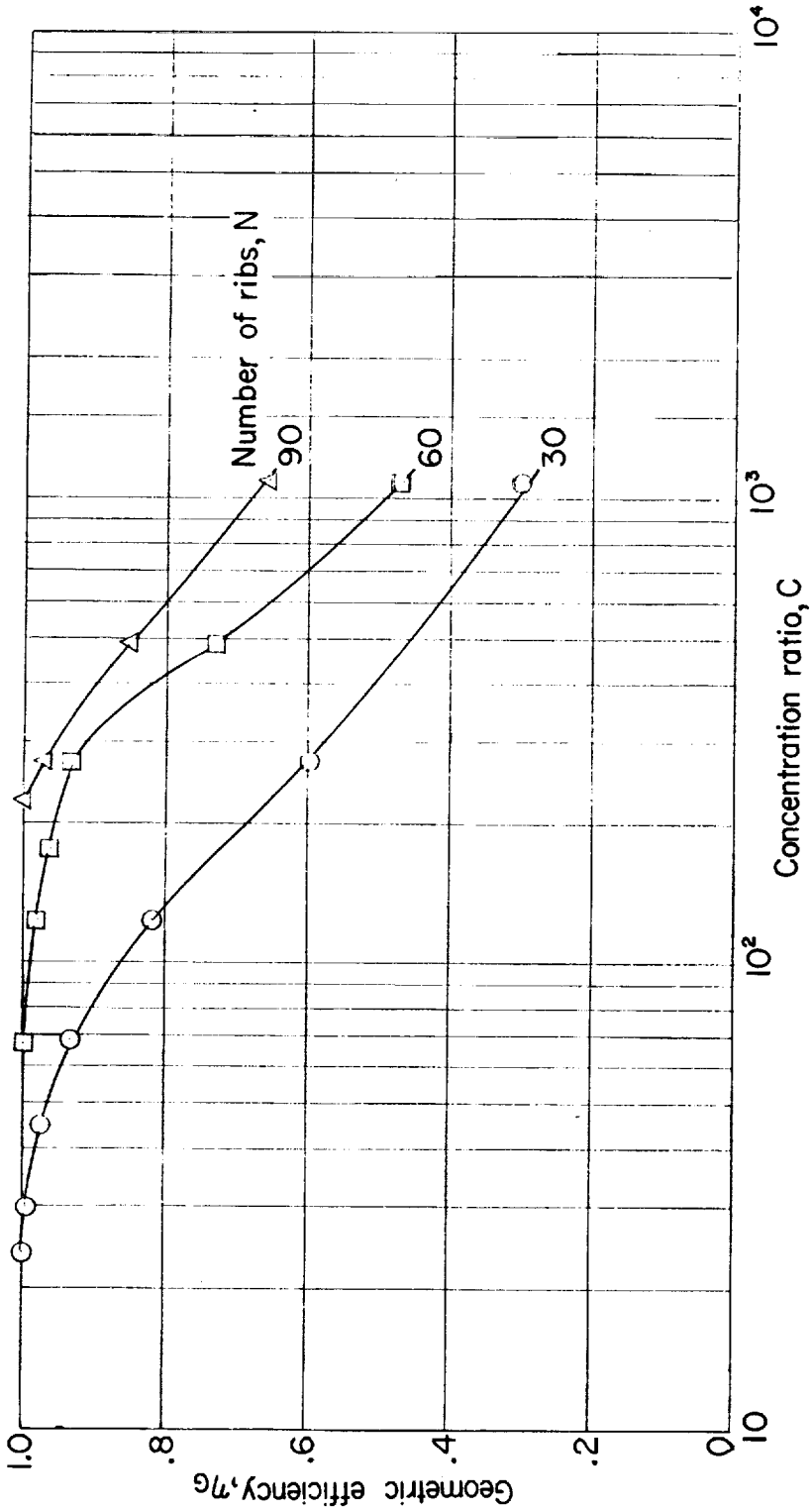

(a) Rim angle 90°; $\frac{R}{f} = 2.0$.

Figure 5.- A typical variation of geometric efficiency with concentration ratio.

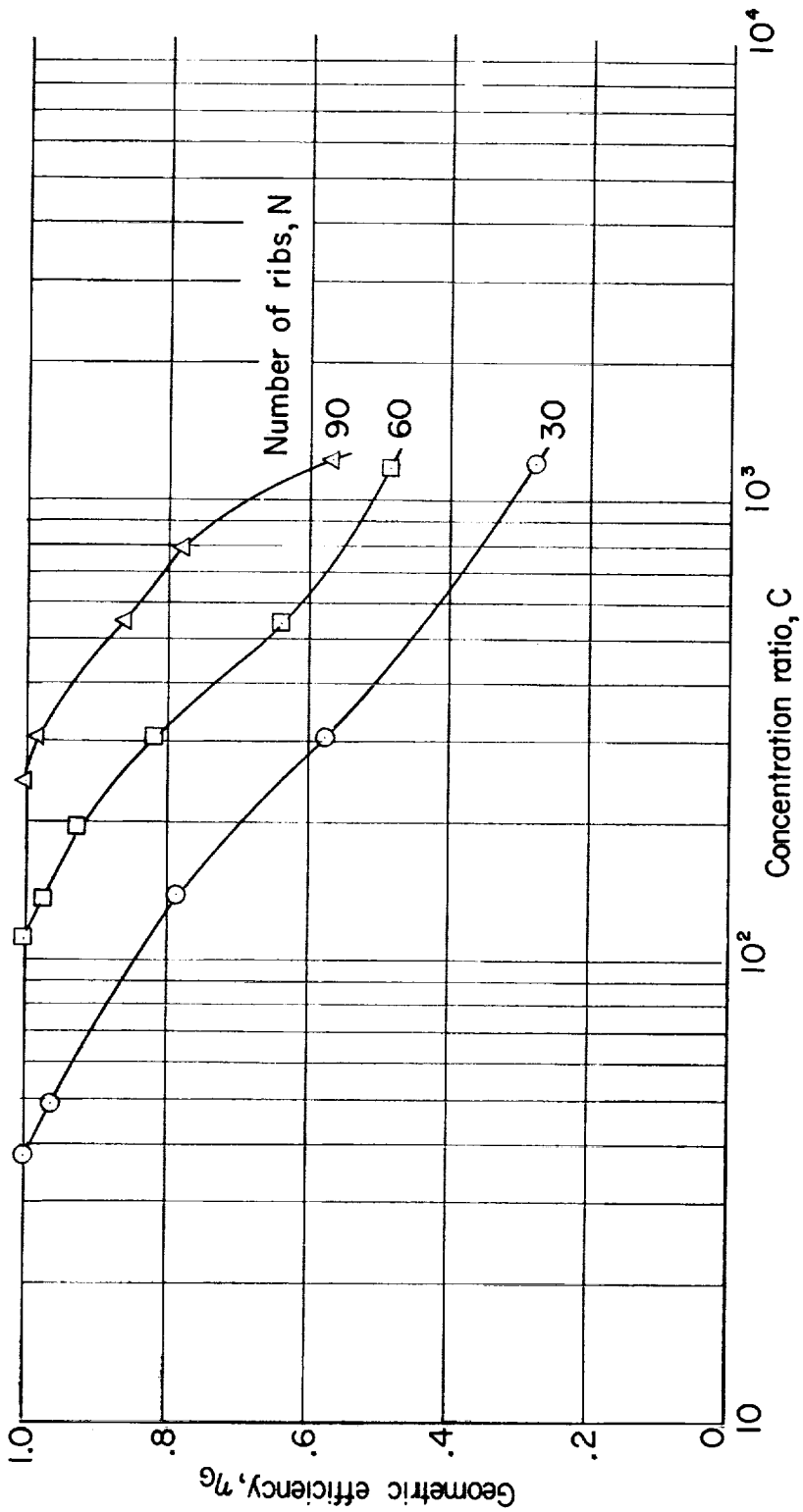

(b) Rim angle 45°; $\frac{R}{f} = 0.829$.

Figure 5.- Concluded.

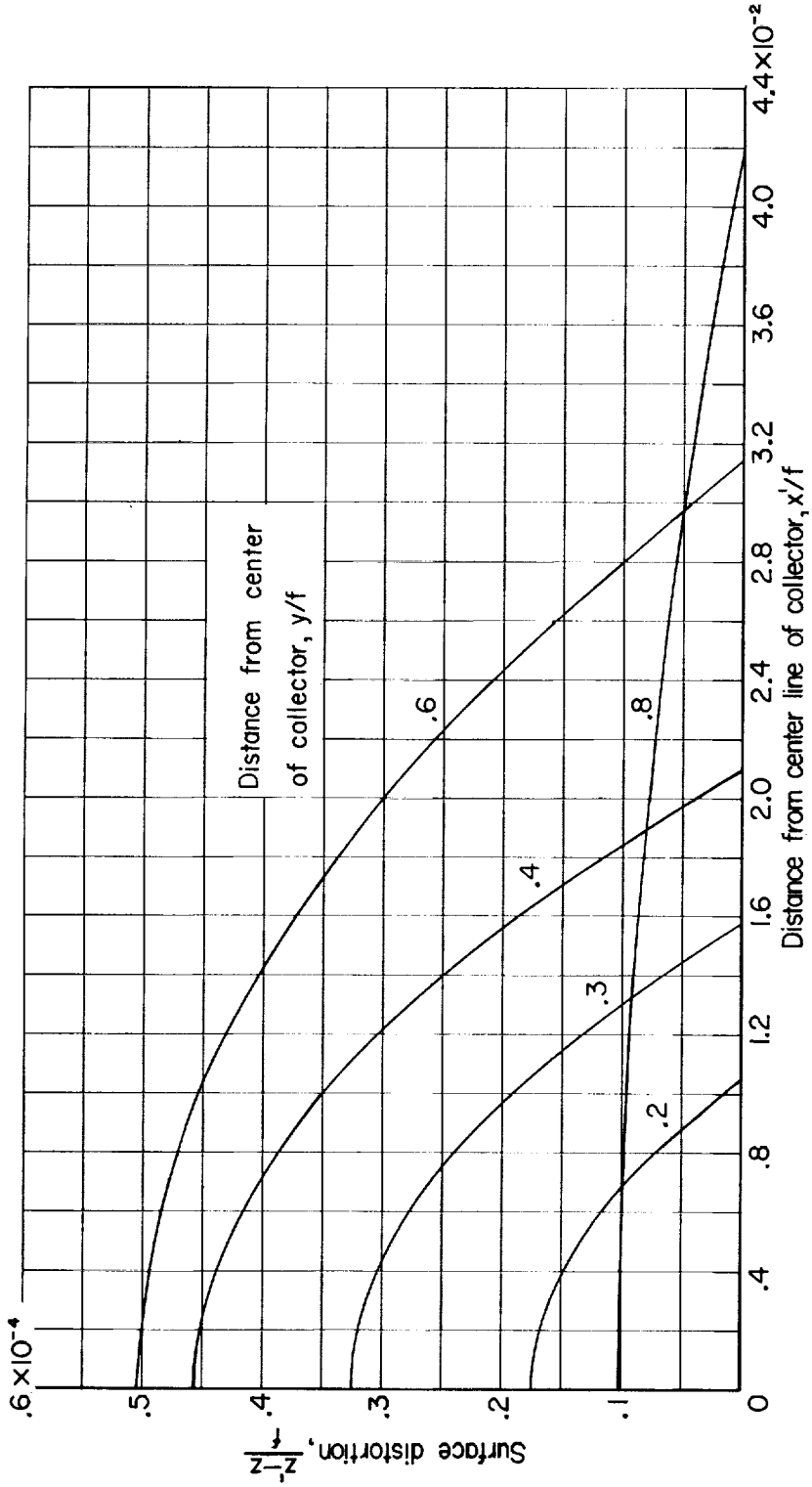

Figure 6.- Surface contours from a segment of a 60-rib collector. Rim angle = 45°; stress-geometry parameter = 1.00.

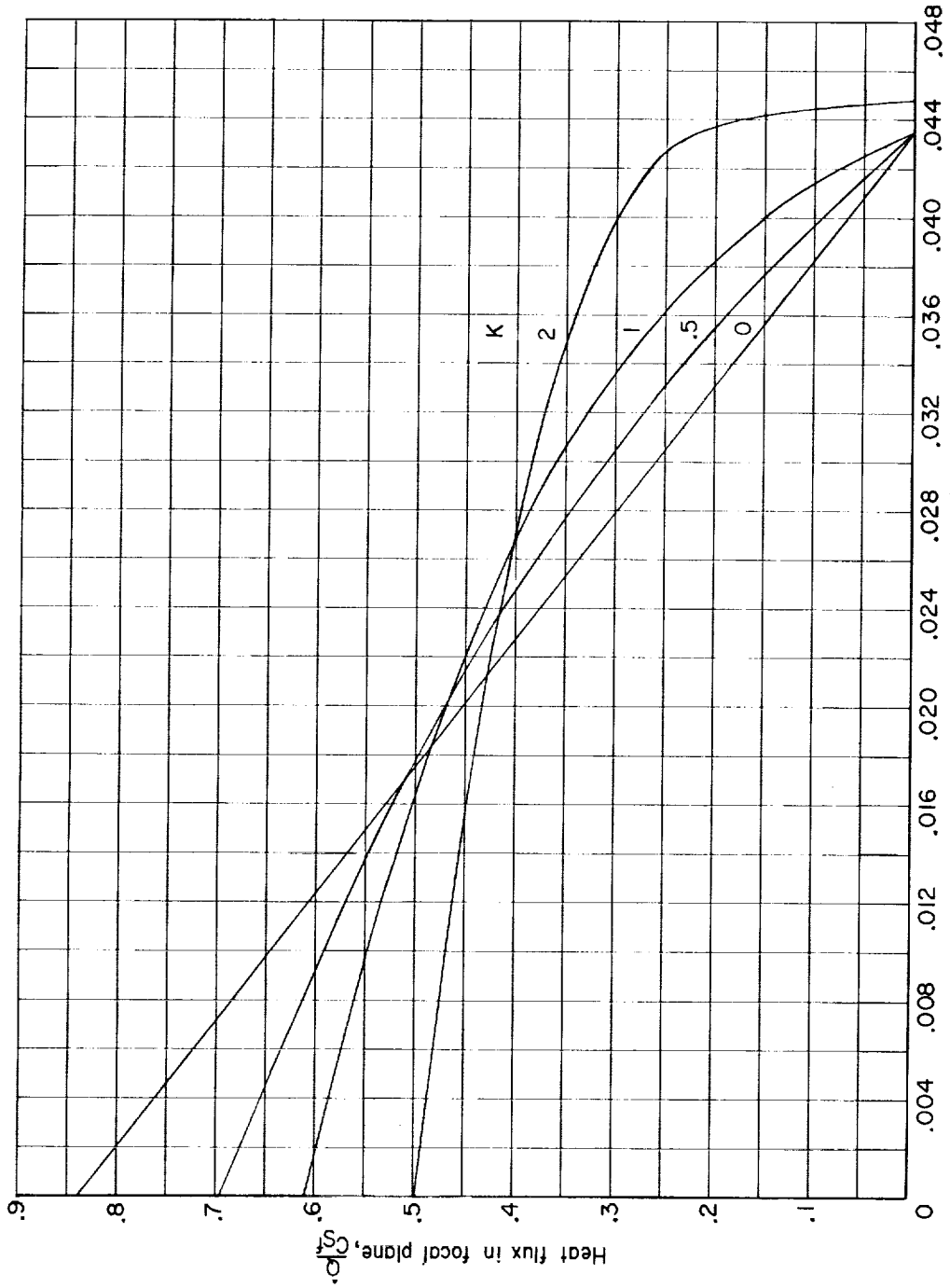

Figure 7.- A typical calculated distribution of heat flux along a radius in the focal plane. $N = 60$; $\frac{R}{f} = 0.829$.

L-1309

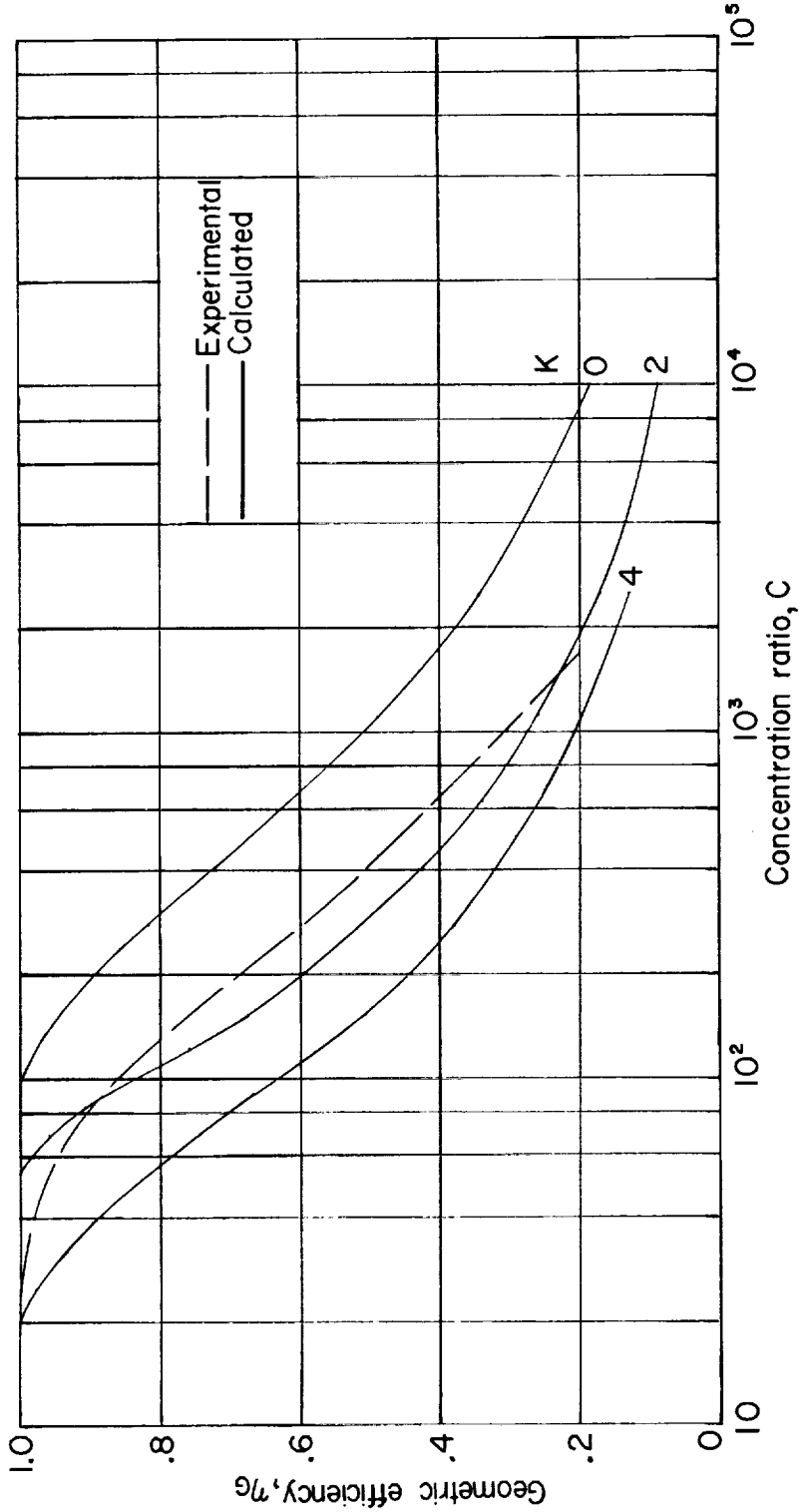

(a) N = 30; $\theta = 90°$; $\frac{R}{f} = 2$.

Figure 8.- Comparison of experimental and calculated geometric efficiency.

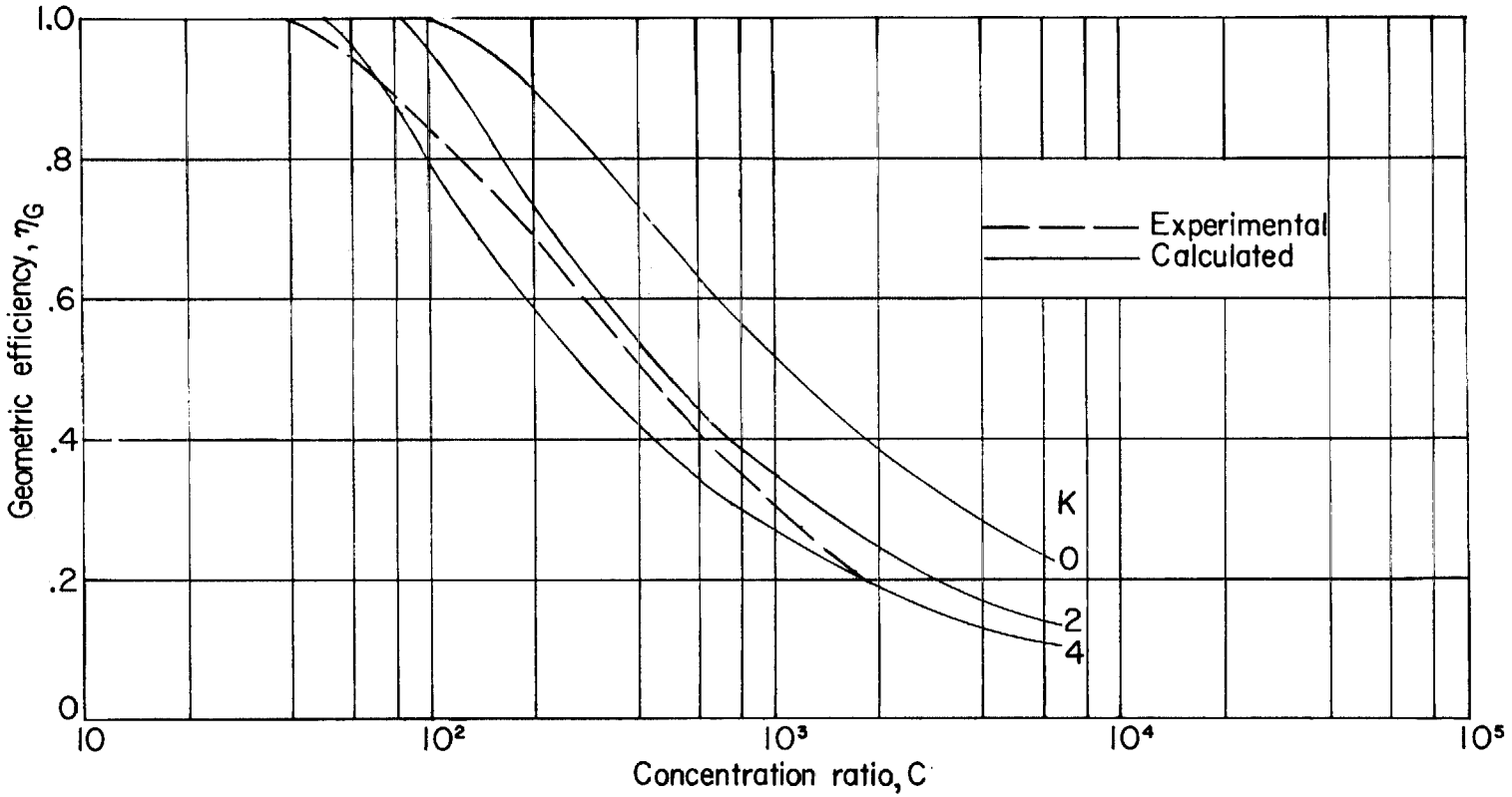

(b) $N = 30$; $\theta = 45^\circ$; $\frac{R}{f} = 0.829$.

Figure 8.- Continued.

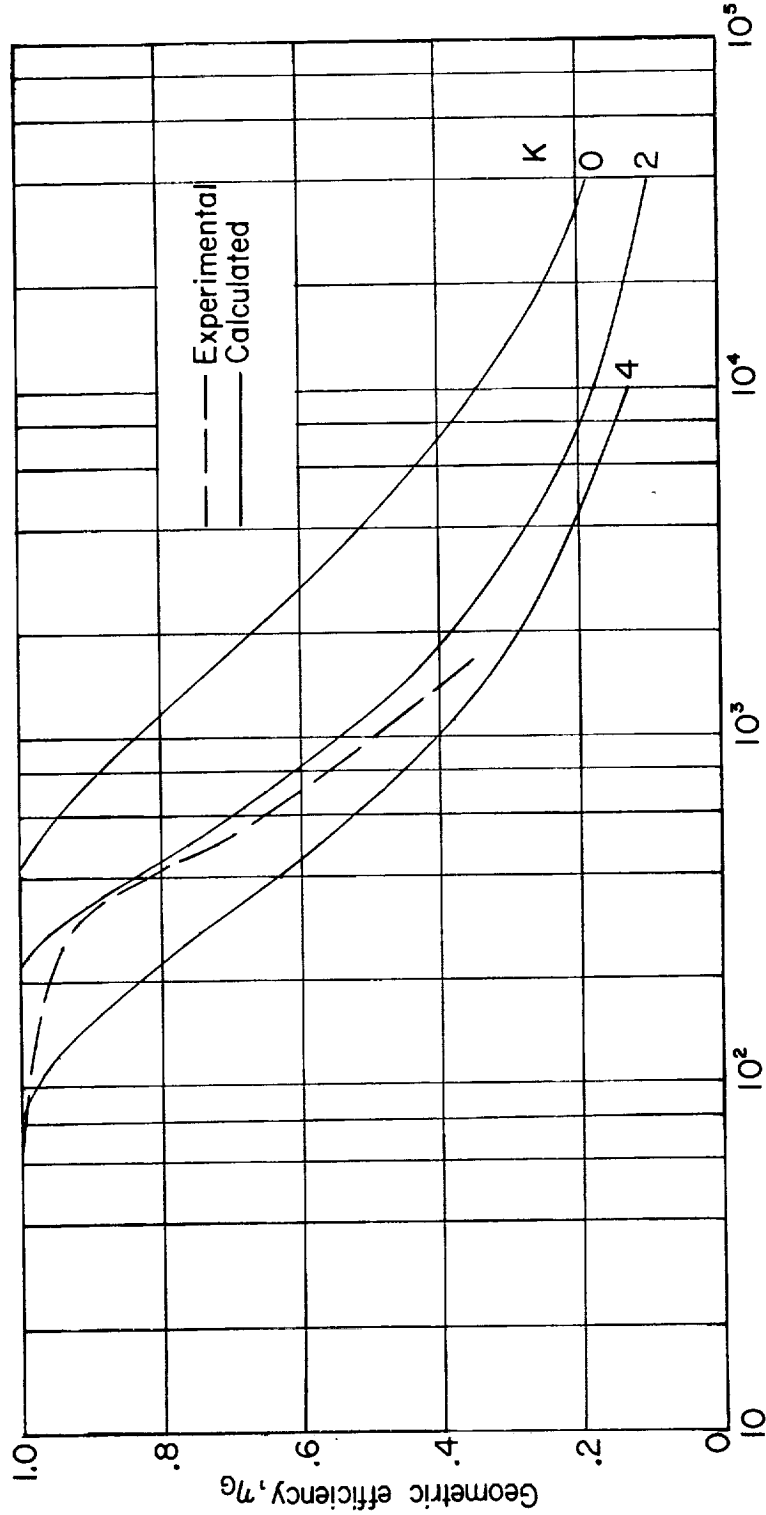

(c) $N = 60$; $\theta = 90°$; $\frac{R}{f} = 2$.

Figure 8.- Continued.

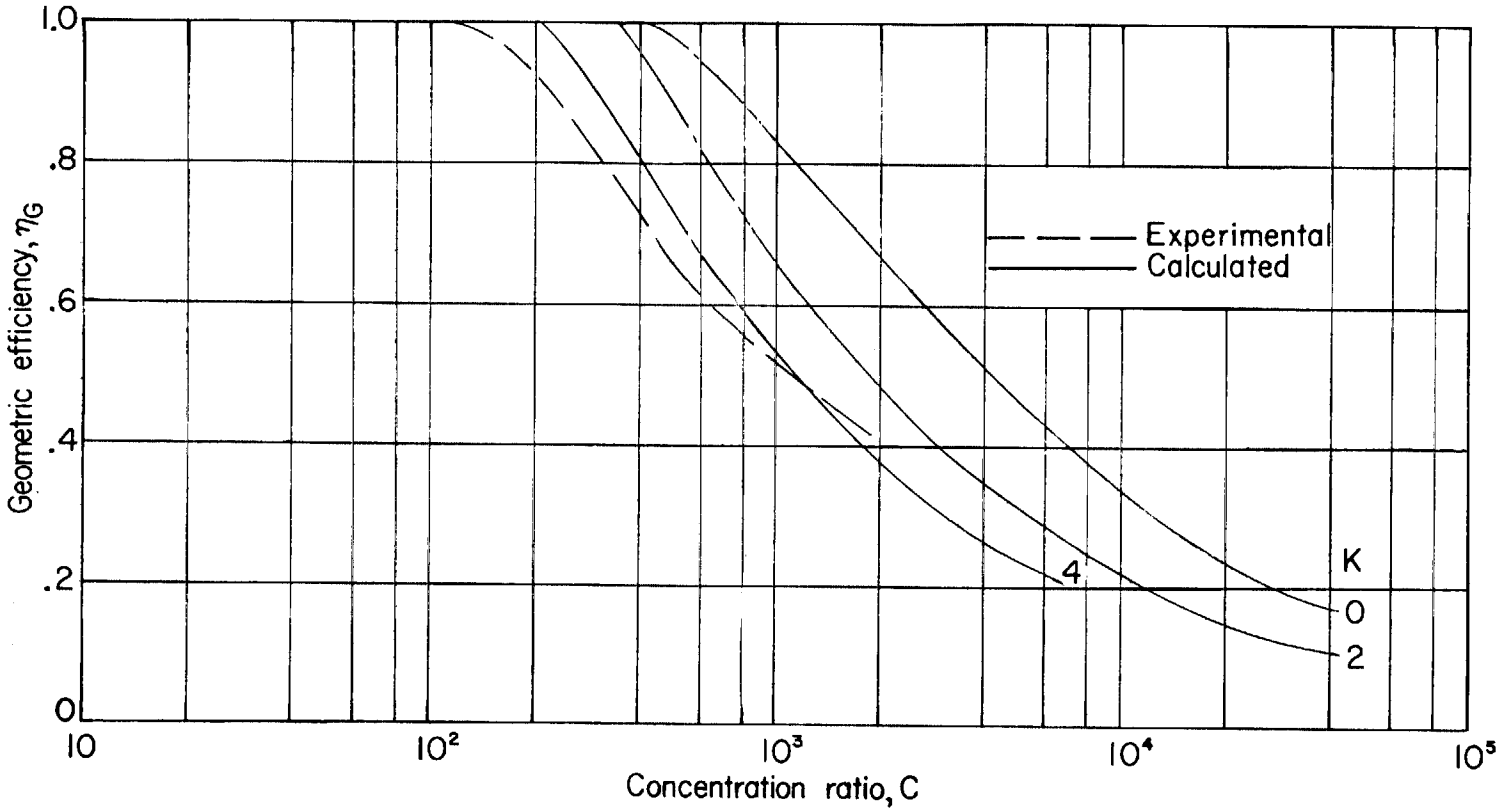

(d) N = 60; θ = 45°; $\frac{R}{f}$ = 0.829.

Figure 8.- Continued.

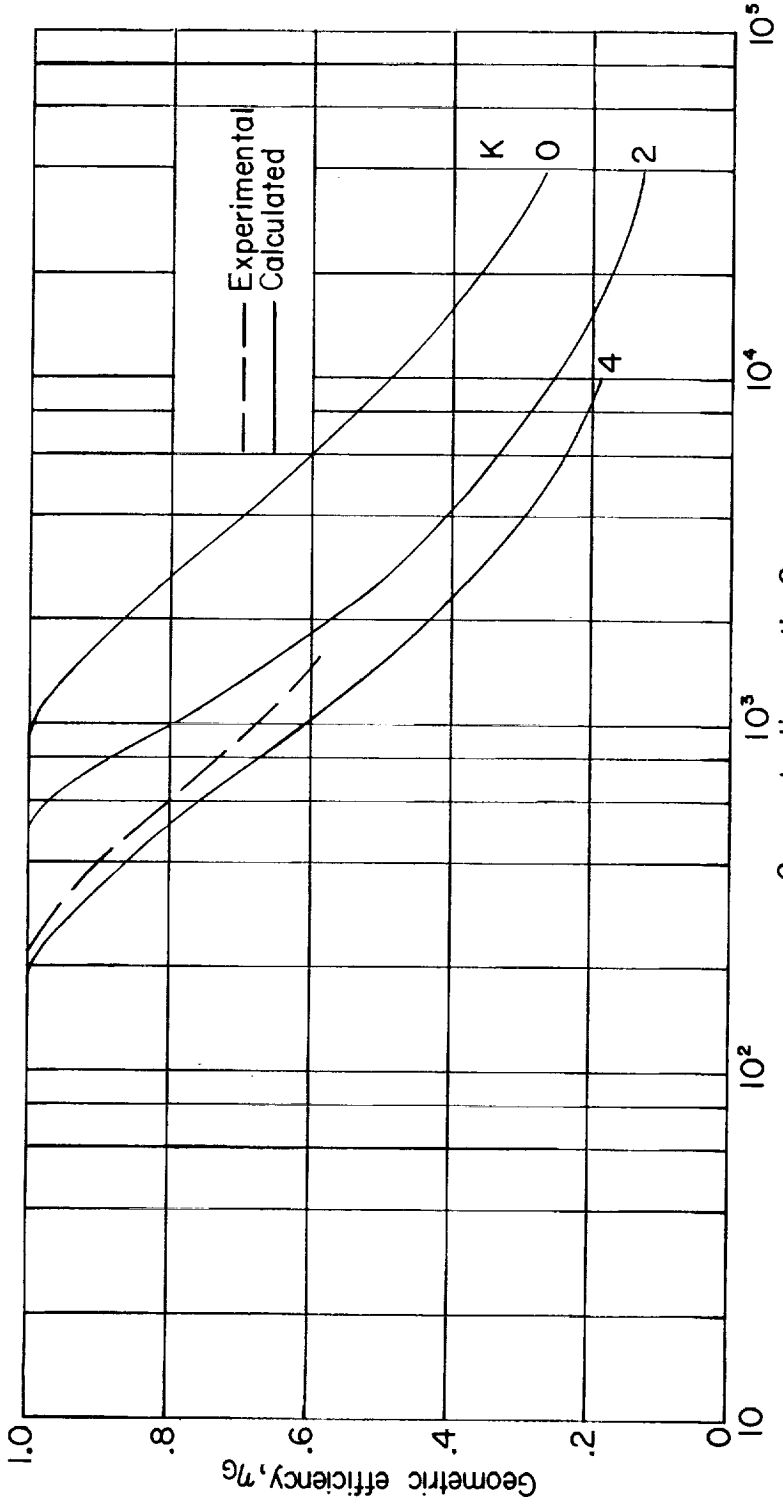

(e) $N = 90$; $\theta = 90°$; $\frac{R}{f} = 2$.

Figure 8.- Continued.

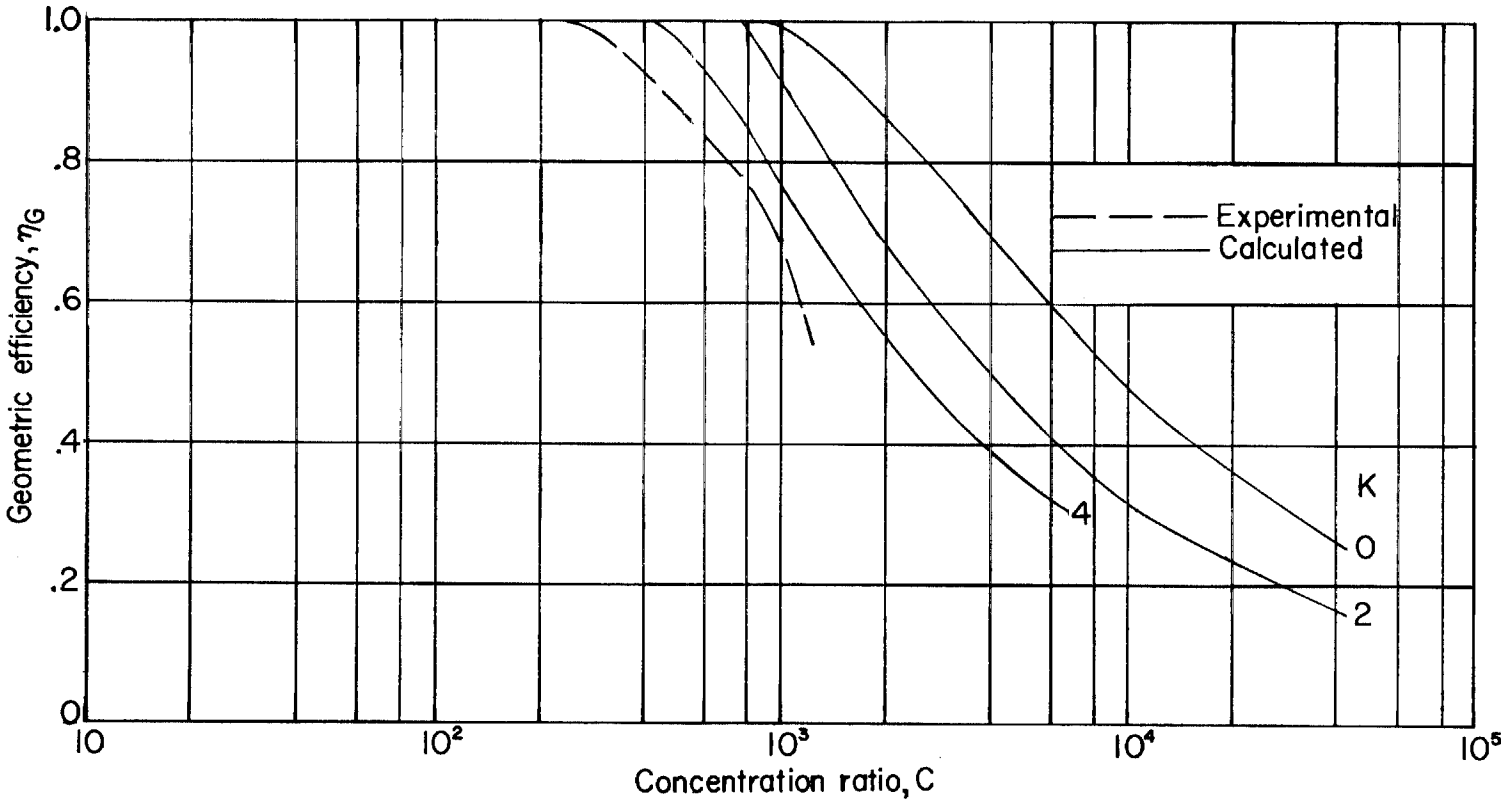

(f) $N = 90$; $\theta = 45^\circ$; $\frac{R}{f} = 0.829$.

Figure 8.- Concluded.

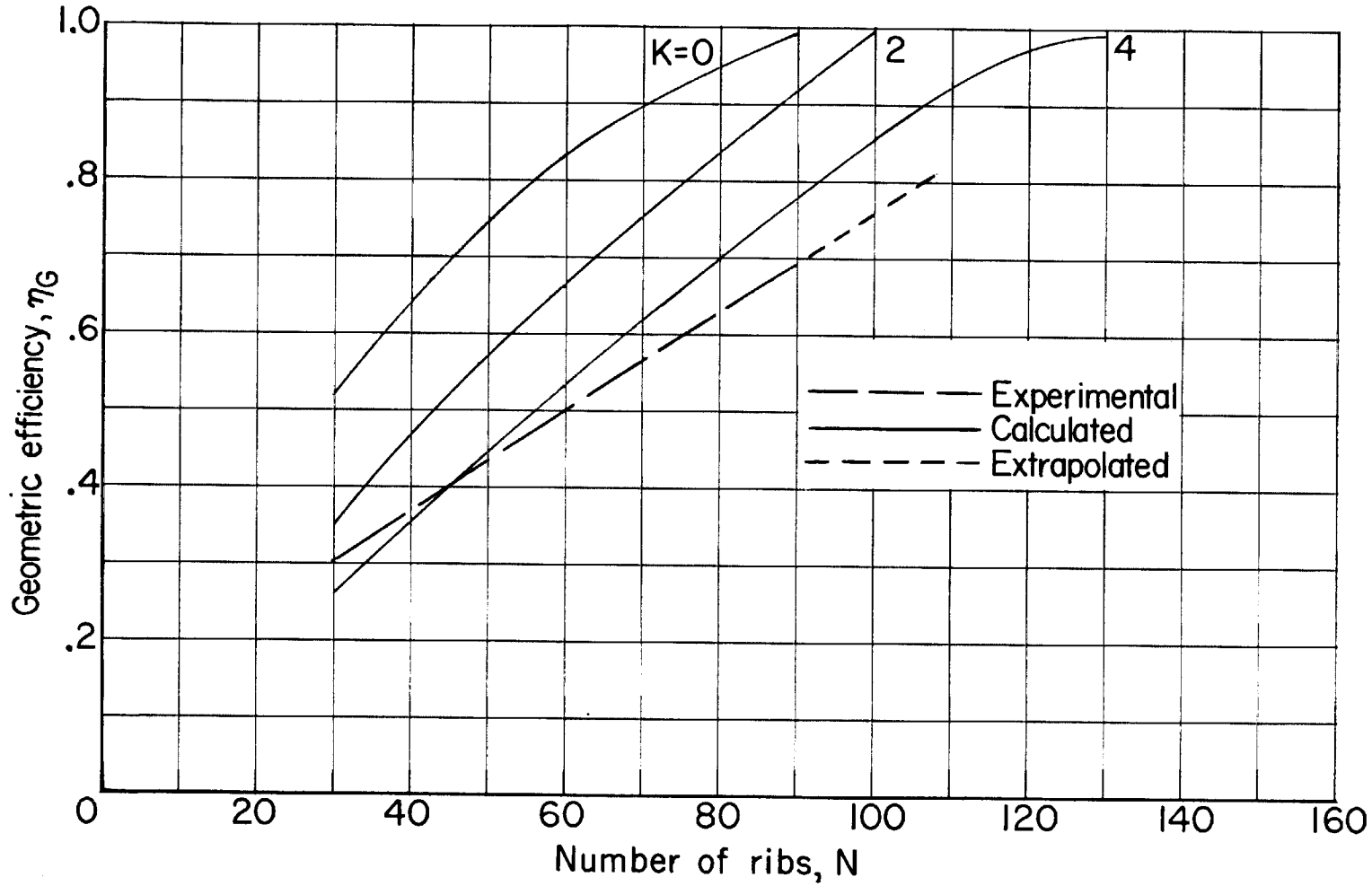

(a) C = 1,000; $\theta = 45^\circ$; $\frac{R}{f} = 0.829$.

Figure 9.- Variation of geometrical efficiency with number of ribs at a concentration of 1,000.

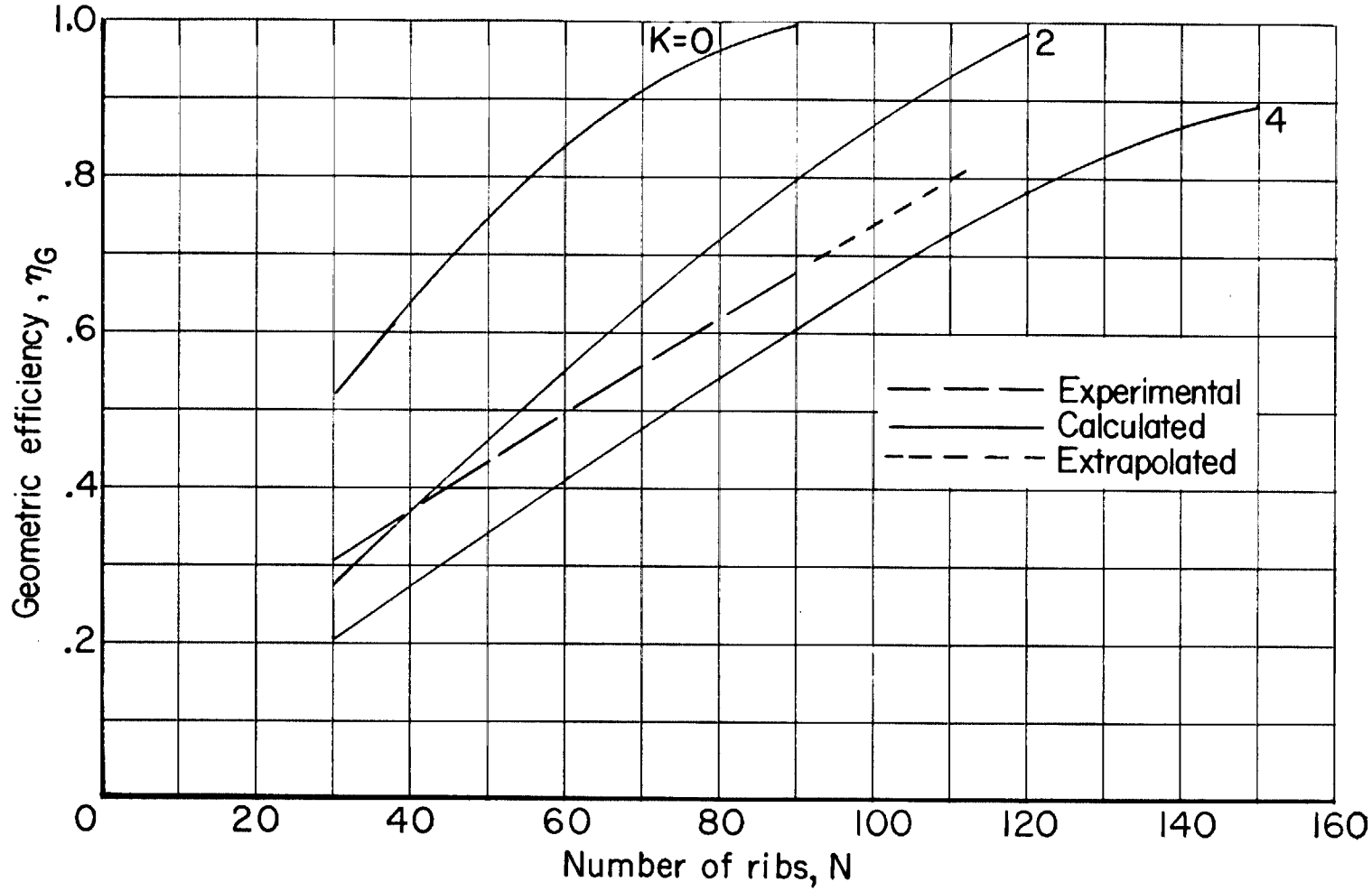

(b) $C = 1{,}000$; $\theta = 90^\circ$; $\frac{R}{f} = 2$.

Figure 9.- Concluded.